

A lysine-restricted diet ameliorates obesity via enrichment of *Parabacteroides goldsteinii* and 1,4-methylimidazoleacetic acid

Received: 24 September 2024

Accepted: 30 September 2025

Published online: 12 November 2025

 Check for updates

Feng Zhao^{1,2,7}, Zhen Zou^{3,7}, Zhaoyi Liu^{1,2,7}, Jiao Wang^{1,2,7}, Yuehua Wu^{1,2,7}, Jun Zhang^{3,7}, Qin Liu^{2,4}, Weijuan Liang^{1,2}, Jinwen Yao^{2,5}, Xuejun Jiang², Michael N. Routledge⁶, Ahmad Khan^{2,5}, Hongyang Zhang^{1,2}, Jingfu Qiu^{1,2} & Chengzhi Chen^{2,5}✉

The effects of dietary amino acid restriction on obesity may be related to the gut microbiome, but its role and mechanism in lysine-restricted diet (LRD) on childhood obesity is largely undefined. Herein, we show that blood lysine levels are elevated in children with obesity compared to healthy controls. Using young mice, we show that LRD ameliorates obesity via gut microbiota modulation. We further identify *Parabacteroides goldsteinii* (*P. goldsteinii*) as a candidate contributor and validate that its supplementation reduces obesity phenotype. Metabolomics reveals that *P. goldsteinii* increases 1,4-methylimidazoleacetic acid (MIAA), a metabolite linked to decreased body weight in animal models. Mechanistically, we show that MIAA inhibits the expression of the demethylase FTO, leading to increased m⁶A modifications on *Slc2a4* mRNA via the reader protein YTHDC1. Collectively, these findings suggest a role for *P. goldsteinii* and its metabolite MIAA on LRD-mediated obesity reduction, potentially via the FTO-SLC2A4 axis to restrict adipose tissue expansion.

Childhood obesity is a major global public health issue. By 2050, 746 million children and adolescents are estimated to be affected by obesity globally¹. Compared with normal-weight children, overweight or children with obesity are at a greater risk of developing metabolic diseases such as diabetes, and cardiovascular diseases². Childhood obesity is characterized by unique physiological vulnerabilities and behavioral-social determinants, with longitudinal cardiometabolic risks necessitating growth-conscious interventions^{3,4}. Many factors can lead to childhood obesity, including genetics, environmental factors, and diet, with the latter being currently recognized as one of the most influential factors⁵. Excessive calorie intake can lead to pathological

weight gain and fat accumulation⁶. Dietary restriction (DR) may serve as an excellent intervention approach to enhance metabolism and boost human health^{7,8}. DR methods mainly include energy restriction, protein restriction (PR), and intermittent fasting⁹. A prior study revealed that while the timing of daily caloric intake did not alter the energy metabolism of individuals with obesity, it did influence their appetite and hunger responses¹⁰. However, a low-fat diet (LFD) may lead to insufficient dietary fat intake, including unsaturated fatty acids¹¹, which are critical for respiratory and neurodevelopmental health in infants and adolescents^{12,13}. Furthermore, inadequate dietary fat intake can impair the absorption of fat-soluble vitamins, potentially

¹Department of Health Laboratory Technology, College of Public Health, Chongqing Medical University, Chongqing, People's Republic of China. ²Research Center for Environment and Human Health, College of Public Health, Chongqing Medical University, Chongqing, People's Republic of China. ³Molecular Biology Laboratory of Respiratory Disease, Key Laboratory of Clinical Laboratory Diagnostics (Ministry of Education), College of Laboratory Medicine, Chongqing Medical University, Chongqing, People's Republic of China. ⁴Research Center for Medicine and Social Development, College of Public Health, Chongqing Medical University, Chongqing, People's Republic of China. ⁵Department of Occupational and Environmental Health, College of Public Health, Chongqing Medical University, Chongqing, People's Republic of China. ⁶Leicester Medical School, University of Leicester, Leicester, UK. ⁷These authors contributed equally: Feng Zhao, Zhen Zou, Zhaoyi Liu, Jiao Wang, Yuehua Wu, Jun Zhang. ✉e-mail: chengzhichen@cqmu.edu.cn

causing skeletal deformities, blindness, bleeding disorders, and neurological damage in children^{14,15}. More importantly, clinical studies have shown that PR can improve a body's metabolic status, thereby enhancing its insulin sensitivity and reducing obesity¹⁶. Additionally, PR has been shown to improve the metabolic status and prolong the lifespan of rodents^{17,18}.

The gut microbiota plays key roles in maintaining the gastrointestinal microecological environment. Gut microbiota can metabolize dietary nutrients and influence many physiological processes, including fat accumulation and blood glucose metabolism^{19,20}. The structure and function of the gut microbiota can be influenced by various factors, including host genetics²¹, antibiotics²², and diet²³. Murine studies indicate that DR remodels the gut microbiota composition/function via reduced intake or nutrient alteration, thereby ameliorating obesity and metabolic dysregulation²⁴. Clinical research has also revealed that long-term DR maintains a healthy metabolic level by reducing the ratio of Firmicutes to Bacteroidetes and enriching anti-inflammatory microbial communities in the gut²⁵. Therefore, it is generally believed that changes in dietary structures can play a significant physiological regulatory role by regulating the levels of intestinal microbiota and metabolites. Study also suggests that the gut microbiota plays important roles in mediating weight loss and improving the host metabolic profile related to DR^{26,27}. Furthermore, some scholars have proposed that selectively reducing specific essential amino acids can improve an organism's metabolism, regardless of its total protein and calorie intake. For example, it has been reported that restricting essential amino acids^{28–31} in the diet of experimental mice can effectively reduce energy expenditure and food intake, and even counteract the fat accumulation and insulin resistance induced by a high-fat diet (HFD) in obese mice. Emerging evidence further suggests amino acid-restricted diets remodel gut microbiota composition, ameliorating obesity and inflammation in HFD-fed mice³².

Lysine, an essential amino acid, is only absorbed in its L-form by biological entities. Upon ingestion, lysine enters small intestinal mucosal cells from the intestinal lumen via active transport and then travels to the liver through the portal vein³³. Study has confirmed that lysine participates in the synthesis of various proteins and fat metabolism in the body³⁴. Lysine not only maintains metabolic homeostasis but may also be associated with childhood growth and development, as it plays critical roles in enhancing immune function, promoting brain and physical maturation, improving nutritional status, and stimulating appetite³⁵. Therefore, prolonged adherence to lysine-restricted diet (LRD) in healthy children may lead to potential developmental impairments. However, whether an LRD can contribute to weight loss remains unclear. Therefore, in this study, we investigated the impact of an LRD on the phenotypes of childhood obesity. We elucidated, from the perspective of the gut microbiota, the mechanisms underlying the anti-obesity effects of LRD. Additionally, we discovered and characterized a bacterial strain, *Parabacteroides goldsteinii* (*P. goldsteinii*), that protected against childhood obesity, and obtained clear evidence that *P. goldsteinii* enhanced the level of 1,4-methylimidazoleacetic acid (MIAA). MIAA is an endogenous biomarker and metabolite of histamine turnover³⁶. Mechanistic studies show that MIAA supplementation increases the m⁶A modification levels of solute carrier family 2 member 4 (*Slc2a4*) mRNA by inhibiting fat mass and obesity-associated protein (FTO), an RNA demethylase that removes m⁶A modifications³⁷. This inhibition reduces FTO expression, thereby elevating m⁶A levels on *Slc2a4* mRNA. The m⁶A modifications are recognized by the YTH N⁶-methyladenosine RNA-binding protein C1 (YTHDC1). This pathway improves glucose metabolism and reduces adiposity, ultimately lowering body weight. To enhance the resistance of *P. goldsteinii* to gastric acid and digestive enzymes, we also formulated an innovative microencapsulation treatment and found that encapsulated *P. goldsteinii* had a significantly

enhanced anti-obesity effect. These findings will provide new strategies and ideas for the treatment of childhood obesity.

Results

LRD ameliorates the obesity phenotype in young mice fed with HFD

This study included 30 children with obesity and 30 healthy controls assigned to groups on the basis of their body mass index (BMI) (Fig. 1a and Supplementary Table 1). We discovered a considerable rise in the level of lysine in the plasma of children with obesity compared to that in healthy controls (Fig. 1b). Moreover, plasma lysine levels were positively correlated with the children's BMI and homeostatic model assessment of insulin resistance (HOMA-IR) score (Fig. 1c, d). Therefore, we speculated that a higher intake of lysine may be one of the risk factors for childhood obesity.

Based on these findings, we first established HFD and LFD mouse models fed with LRD. We conducted 40% and 80% LRD experiments in mice fed an LFD or an HFD to compare the effects of LRD on the body weights of normal and obese mice (Fig. 1e and Supplementary Fig. 1a). We did not observe weight loss effects with the 40% LRD regimen. Furthermore, neither the LRD regimen significantly altered the body weights of mice in the LFD group. Only the 80% LRD significantly reduced the body weights of obese mice fed a HFD, and this weight loss required at least 8 weeks of LRD to be achieved (Fig. 1f–h and Supplementary Fig. 1b–g). To assess the effects of LRD on the intrinsic nutritional status of mice, we monitored oxygen consumption (VO₂) and validation of carbon dioxide production (VCO₂) using metabolic cages to calculate the respiratory exchange ratio (RER) and energy expenditure (EE). The results demonstrated that HFD-fed mice exhibited significantly reduced VO₂, VCO₂, and EE, particularly during the dark (active) phase, with no notable impact of LRD intervention on VO₂ or EE in HFD-fed mice, further analysis revealed that changes in RER followed consistent trends across all experimental groups (Fig. 1i–m and Supplementary Fig. 1h–j). Similarly, LRD intervention showed no significant effects on ambulatory activity or fecal triglyceride levels in mice (Fig. 1n and Supplementary Fig. 1k). These findings suggest that the weight-reducing effects of LRD intervention are not directly associated with the intrinsic nutritional status but are instead linked to ameliorated systemic insulin resistance of the animals (Fig. 1o–t). Subsequently, we found that while the 80% LRD intervention did not reduce liver weight in HFD-fed mice, it effectively ameliorated hepatic lipid accumulation and concurrently improved abnormal blood lipid profiles (Fig. 1u, v and Supplementary Fig. 1l). Furthermore, we observed that 80% LRD significantly decreased epididymal white adipose tissue (eWAT) mass and reduced adipocyte size in HFD mice (Supplementary Fig. 1m–o). Additionally, the weight loss effect of 80% LRD was also observed in the *Leptin* knock out (KO) mouse models (Supplementary Fig. 2a–p). Next, we compared the weight loss effects of the 80% LRD with those of the weight loss drug orlistat (Supplementary Fig. 3a). We found that the 80% LRD achieved a weight loss efficacy similar to that of orlistat. However, we did not observe any synergistic effects when both treatments were administered concurrently (Supplementary Fig. 3b–p).

LRD ameliorates intestinal microecological disturbances in obese mice

Building on the established role of the intestine in dietary essential amino acid metabolism and the link between amino acid absorption and gut microbiota stability, we observed significant dysbiosis in HFD-fed mice, characterized by elevated α -diversity indices; notably, 80% LRD intervention attenuated this increase in α -diversity (Fig. 2a), but as revealed by PCoA analysis, exerted no discernible effect on β -diversity (Fig. 2b) while distinctly altering the relative abundance of species (Fig. 2c). Furthermore, 80% LRD intervention was observed to significantly ameliorate intestinal barrier injury in the two obese mouse

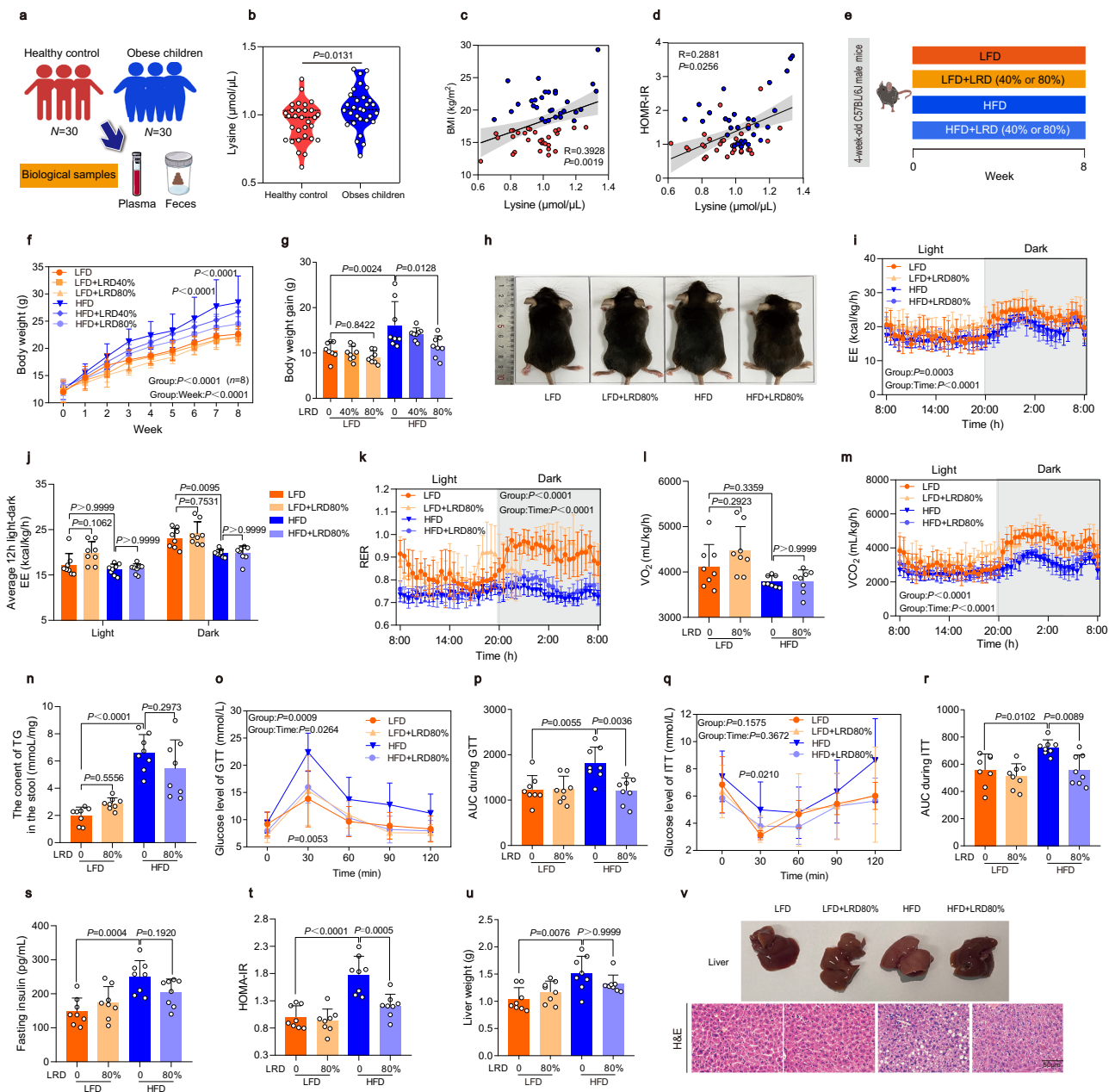


Fig. 1 | The LRD demonstrates significant efficacy against obesity in young mice fed with HFD. **a** Flow chart of the population survey. **b** Comparison of serum lysine concentration between healthy control and children with obesity. **c, d** Correlation of serum lysine concentration with body mass index (BMI) and homeostatic model assessment of insulin resistance (HOMA-IR) in children and linear regression lines with 95% confidence intervals. **e** Flow chart of the animal experiments. **f–h** Body weight, body weight gain and the body size of mice in each group over the course of the 8-week experiment. **i** Energy expenditure (EE) fluctuations in mice during light and dark cycles with different diets. **j** EE during light and dark periods in mice on different diets. **k** Respiratory exchange ratio (RER) fluctuations in mice during light and dark cycles with different diets. **l** Oxygen consumption (VO_2) measurements for mice on varied dietary conditions. **m** Carbon dioxide production (VCO_2) measurements for mice on varied dietary conditions over time. **n** Measurement of triglyceride (TG) content in stool across different dietary groups. **o–r** Glucose

metabolism of mice in each group at the end of the experiment including intraperitoneal glucose tolerance test (GTT) with the area under curve (AUC) of GTT, intraperitoneal insulin tolerance test (ITT) with AUC. **s, t** Fasting insulin and HOMA-IR. **u** Weight of liver. **v** Liver morphology and H&E-stained sections (representative images) (scale bars, 50 μ m) in mice exposed to different diets. Each dot represents a child volunteer (**b–d**) ($N=30$ per group). P values were calculated with the unpaired two-tailed Student's t test (**b**), *Pearson* and *Spearman* correlation analysis (two-tailed) (**c, d**). Each point in graphs (**g, j, l, n, p, r–u**) represents the value obtained in an independent mouse ($n=8$, per group). Data were presented as mean \pm S.E.M. P values were calculated with the two-way repeated-measure ANOVA (**f, i, k, m, o, q**), one-way ANOVA followed by Tukey's post-hoc analysis (**g, l, n, p, r–t**), Kruskal-Wallis test followed by Dunn's post-hoc analysis (**j**) and exact P value were shown in figure panels. Source data are provided in a Source data file.

models (Fig. 2d and Supplementary Fig. 4a–h). Therefore, we utilized the gastric intervention of an antibiotic mixture (ABX) solution to simulate a germ-free like mouse model (Supplementary Fig. 4i). The results demonstrated that ABX intervention for two weeks exerted no discernible impact on the phenotype of HFD-fed mice; moreover,

concurrent administration with 80% LRD yielded no additive effect (Supplementary Fig. 4j–p).

We subsequently collected fecal samples from individuals with obesity and healthy control children to establish a human fecal microbiota transplantation (FMT) mouse model (Supplementary

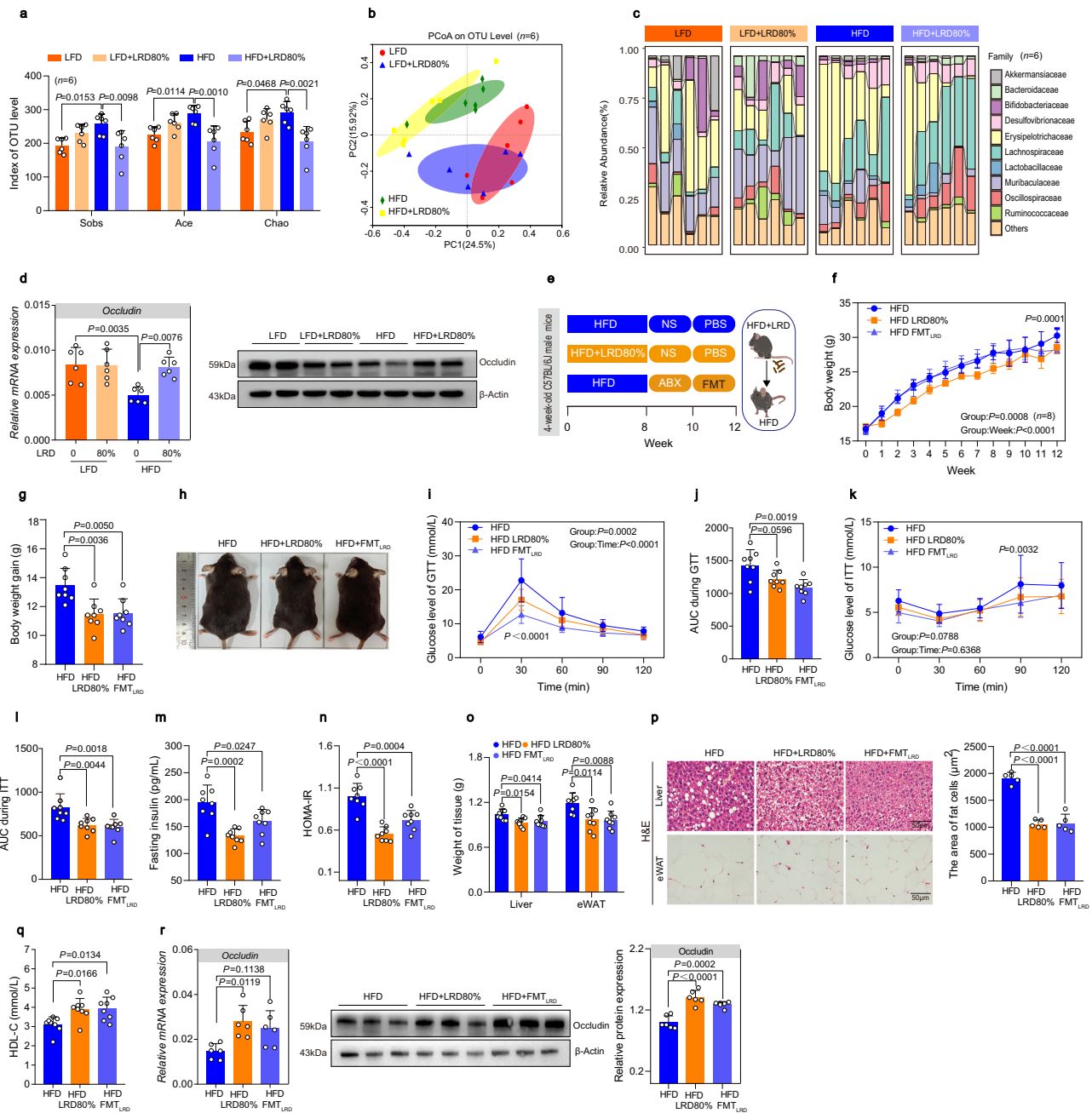


Fig. 2 | Gut microbiota plays an important role in anti-obesity with LRD. **a** The α diversity of gut microbiota from different groups at the end of dietary treatment was measured by Sobs, Ace and Chao index on OTU levels. **b** PCoA plot based on Bray-Curtis dissimilarity matrices of gut microbiota in mice treated with different diets. The data were compared by the Adonis test. **c** Relative abundance of bacteria in the gut microbiota of mice treated with different diets at the family level. **d** Left: mRNA expression of *Occludin* in indicated mice by RT-qPCR ($n = 6$ per group). Right: representative blots ($n = 2$ per group). **e** Schematic diagram of experimental strategy for FMT. **f, g** The body weight and body weight gain of mice in each group. **h** Differences in body size of mice between each groups after 2 weeks of FMT. **i-l** Glucose metabolism of mice in each group at the end of experiment including GTT, AUC of GTT, ITT and AUC of ITT. **m, n** Fasting insulin and HOMA-IR. **o** The weights

of liver and eWAT of mice among each group after the 12-week experiment. **p** Pathological changes in the liver and eWAT of mice exposed to different treatments for 12 weeks, including H&E stained sections (representative images) (scale bars, 50 μm) and the area of fat cells. **q** Level of HDL-C in plasma of mice after 12 weeks of exposure to different treatments. **r** Left: mRNA expression of *Occludin* in indicated mice by qRT-PCR. Middle: representative blots. Right: Western blot analysis of *Occludin* expression in tissues from indicated mice ($n = 6$ or 3 per group). Each point in graphs (**a, b, g, j, l-o, q**) represents the value obtained in an independent mouse ($n = 6$ or 8 per group). Data were presented as mean \pm S.E.M. P values were calculated with the two-way repeated-measure ANOVA (**f, i, k**), one-way ANOVA followed by Tukey's *post-hoc* analysis (**a, d, g, j, l-r**) and exact P value were shown in figure panels. Source data are provided in a Source data file.

Fig. 5a). LFD mice transplanted with feces from children with obesity presented a significantly obese phenotype, while HFD mice transplanted with fecal microbiota from healthy control individuals displayed a significant amelioration of their obese phenotype (Supplementary Fig. 5b-i). In addition, we also observed tissue damage

and decreased barrier function in the colon of HFD group mice, which was alleviated the transplantation of feces from healthy children (Supplementary Fig. 5j-l). These findings further validate how differences in gut microbiota can impact the obesity phenotype. However, whether the dysbiosis of gut microbiota caused by obesity is related to

nutritional lysine levels remained unclear. Therefore, we first determined the effects of LRD on the gut microbiota and intestinal barrier function. To further verify the causal relationship between LRD and changes in the gut microbiota, we transplanted feces from mice on an 80% LRD into HFD mice (Fig. 2e). Our results confirmed that the weight loss, weakening of insulin resistance, lipid level abnormalities were all associated with the restoration of the normal gut microbiota balance and repair of the intestinal barrier (Fig. 2f–r).

LRD increases the abundance of *P. goldsteinii* to achieve anti-obesity effects

Next, using 16s rRNA gene sequencing analysis, we screened for different gut microbiota components at the genus level that might be involved in the anti-obesity effects of LRD. Among all the microbial taxa that responded to the LRD, Parabacteroides exhibited the most significant changes at the genus level. Specifically, the abundance of Parabacteroides significantly decreased in the intestines of HFD mice but recovered after LRD (Supplementary Fig. 6a). We further identified for species level participants and confirmed *P. goldsteinii* to be a key bacterial species (Fig. 3a). In addition, correlation analysis revealed that the abundance of *P. goldsteinii* was significantly negatively correlated with body weight, AUC during the GTT, HOMA-IR, and plasma lysine levels (Fig. 3b–e). Consistent with this finding, 80% LRD intervention elevated the fecal abundance of *P. goldsteinii* in *Leptin*-KO mice; notably, it is noteworthy that children with obesity exhibited significantly reduced levels of this bacterium compared to their healthy counterparts (Fig. 3f, g). These results strongly suggested that *P. goldsteinii* was a key species involved in the anti-obesity effects of LRD. To verify this result, we cultivated and identified *P. goldsteinii* under anaerobic conditions in vitro and assessed its growth curve and colony count (Supplementary Fig. 6b–f). We orally supplemented HFD mice with active *P. goldsteinii* in solution at a concentration of 1.0×10^9 CFU/mL (Fig. 3h). The results demonstrated that supplementation with active *P. goldsteinii* significantly elevated the fecal abundance of this bacterium in HFD-fed mice (Fig. 3i). The results showed that supplementation with *P. goldsteinii* alleviated the body weight of HFD mice, relieved their systemic insulin resistance and abnormal lipid levels (Fig. 3j–t and Supplementary Fig. 6g). Additionally, supplementation with *P. goldsteinii* significantly repaired the intestinal barrier injury in HFD mice (Supplementary Fig. 6h–k). Subsequently, we administered heat-inactivated *P. goldsteinii* to HFD-fed male mice via oral gavage. The results demonstrated that inactivated *P. goldsteinii* failed to ameliorate obesity phenotypes in HFD-fed mice (Supplementary Fig. 6l–s), indicating that only viable *P. goldsteinii* exhibits anti-obesity efficacy.

Given the challenges faced by orally administered bacteria due to exposure to extreme acidity, enzymes, and bile salt degradation prior to reaching the colon, resulting in diminished bioactivity and thus impacting the therapeutic efficacy of probiotics, we undertook the encapsulation of *P. goldsteinii* to ensure the activity of the bacteria before they reached the gut (Supplementary Fig. 7a–e). This involved enhancing its delivery efficiency through surface modification and bacterial packaging to optimize therapeutic outcomes. Our findings indicate that this encapsulation strategy showed significantly enhances the restorative effects of *P. goldsteinii* on the obese phenotype and insulin resistance in mice (Supplementary Fig. 8a–k). Moreover, compared with direct bacterial gavage, oral capsule formulations demonstrate markedly superior therapeutic effects in mitigating intestinal barrier damage in obese mice (Supplementary Fig. 8l–n). We further replicated key experiments in female C57BL/6J mice to evaluate the interventional effects of *P. goldsteinii* supplementation on HFD-fed females. The results revealed the limited efficacy of active *P. goldsteinii* interventions in ameliorating obesity phenotypes in female HFD mice (Supplementary Fig. 9a–i). We repeated key experiments in which active *P. goldsteinii* was supplemented in two juvenile

mice models to directly mimic the physiology of children with obesity. The results showed that active *P. goldsteinii* supplementation improved glucose metabolism and reduced fat accumulation in the two juvenile models (Supplementary Fig. 10a–r), consistent with the results observed in young adult mice.

LRD induces weight loss by enriching the gut with *P. goldsteinii* and enhancing MIAA

Next, we conducted non-targeted metabolomics to observe the differences in mouse serum metabolic profiles caused by different diets (Supplementary Fig. 11a). We screened for key metabolites involved in the remission of obesity caused by LRD and identified a significantly differentially altered metabolite, 1,4-methylimidazoleacetic acid (MIAA) (Fig. 4a). Furthermore, we found that the levels of MIAA were significantly negatively correlated with weight gain, HOMA-IR, the AUC during the GTT and lysine levels in mice (Fig. 4b–e), indicating that the enrichment with MIAA may have been involved in a key pathway through which LRD alleviated the obesity phenotype. To further clarify the relationship between MIAA and *P. goldsteinii*, we analyzed their correlation. We discovered a significant positive correlation between the levels of MIAA in plasma and the abundance of *P. goldsteinii* in feces of mice (Fig. 4f). Importantly, using LC-MS, we detected the presence of MIAA in the culture supernatant of *P. goldsteinii*; whereas this substance was not detected in the sterile control culture medium (Fig. 4g). These results provide further support for *P. goldsteinii* being a key bacterial species responsible for the production of MIAA.

To follow, we applied an oral gavage of MIAA in HFD mice (Fig. 4h). After 4 weeks of MIAA supplementation, we observed a significant decrease in the body weight of the obese mice which was accompanied by a notable reduction in systemic insulin resistance, the normalization of lipid levels (Fig. 4i–s and Supplementary Fig. 11b). Additionally, we observed significant intestinal barrier restoration in obese mice after MIAA supplementation (Supplementary Fig. 11c–e). These results indicated that LRD relieved the obesity phenotype by enriching the gut with *P. goldsteinii* and increasing the production of its metabolites MIAA. We further replicated key experiments in female C57BL/6J mice to evaluate the interventional effects of MIAA supplementation on HFD-fed females. Results revealed limited efficacy of MIAA interventions in ameliorating obesity phenotypes in female HFD mice (Supplementary Fig. 12a–h).

MIAA exerts anti-obesity effects by upregulating *Slc2a4*

To elucidate the molecular mechanism of MIAA's anti-obesity effect, we employed transcriptomic analysis to screen for potential target genes of MIAA. KEGG enrichment analysis indicated that the anti-obesity effects of MIAA and *P. goldsteinii* were both related to the insulin resistance signaling pathway (Fig. 5a). By comparing the expression of genes related to the insulin resistance signaling pathway in the liver of HFD mice, MIAA-supplemented mice, and *P. goldsteinii*-supplemented mice, we found that *Slc2a4* was the only gene that was differentially expressed in all four groups (Fig. 5b). Subsequently, we confirmed that *Slc2a4* mRNA expression levels were significantly decreased in both HFD mice and *Leptin*-KO obese mice. However, 80% LRD significantly increased the expression levels of the *Slc2a4* mRNA in the livers of both obese mouse models (Fig. 5c and Supplementary Fig. 13a). In addition, we established in vitro insulin-resistant cellular model (Supplementary Fig. 14b, c), in which similar effects were observed; Also, these effects were consistent with those in the in vivo models (Supplementary Fig. 14d).

To investigate whether the decline in *Slc2a4* mRNA in obese mice was influenced by the gut microbiota, we transplanted fecal microbiota from individuals with obesity into LFD mice and found a significant decrease in *Slc2a4* mRNA expression levels in the liver. Conversely, HFD mice transplanted with fecal microbiota from healthy volunteers showed significantly increased liver *Slc2a4* mRNA

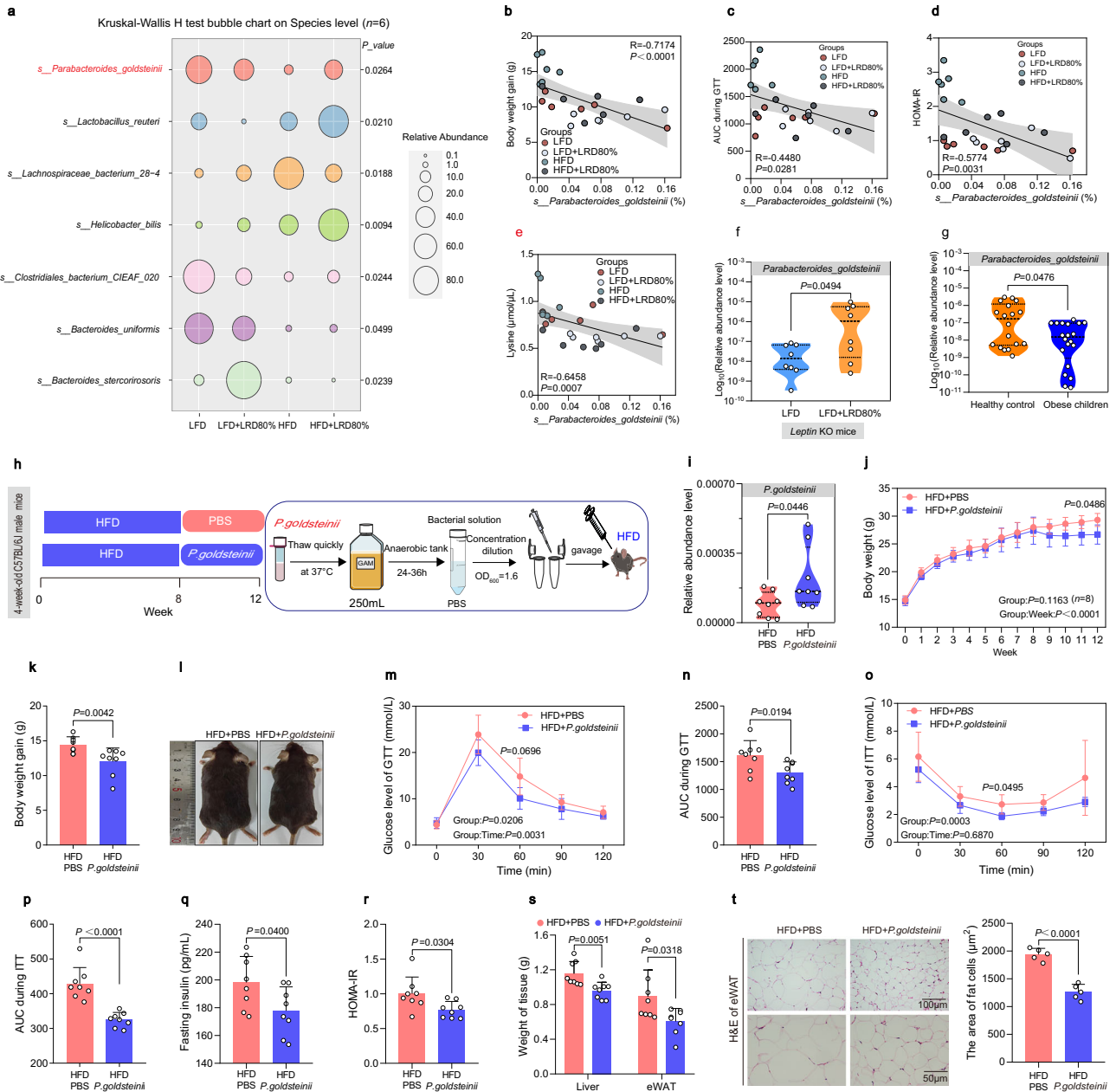


Fig. 3 | *P. goldsteinii* increased as a result of LRD has significant anti-obesity effects. **a** Bubble chart showing the abundance differences of the 7 most abundant species in the fecal microbiota of mice from each group after 8 weeks of different dietary treatment. **b–e** Spearman correlation of the abundance of *P. goldsteinii* in feces with body weight, AUC of GTT, HOMA-IR and plasma lysine concentrations of mice and linear regression line with 95% confidence interval. **f** Differences in the abundance of *P. goldsteinii* in the feces of *Leptin* KO mice. **g** Differences in the abundance of *P. goldsteinii* in feces of healthy controls and children with obesity ($N=18$ or 20). **h** Flow chart of the animal experiments. **i** Differences in the abundance of *P. goldsteinii* in feces of mice at the end of experiment between mice administered with *P. goldsteinii* or PBS. **j** Body weight and body weight gain in each group of mice during the 12-week experiment. **l** Differences in body size of mice between each group after 4 weeks of *P. goldsteinii*/PBS treatment.

m–p Glucose metabolism of mice from each group at the end of experiment including GTT, AUC of GTT, ITT and AUC of ITT. **q, r** Fasting insulin concentrations and HOMA-IR. **s** The weights of liver and eWAT of mice from each group after the 12-week treatment. **t** Pathological changes in the eWAT of mice, including H&E stained sections (representative images) (scale bars, 50 μ m and 100 μ m) and the area of fat cells. Each circle represents an independent experimental group (**a**). Each point in graphs (**b–f**, **i**, **k**, **n**, **p–s**) represents the value obtained in an independent mouse ($n=6$ or 8 per group). Data were presented as mean \pm S.E.M. *P* values were calculated with the Kruskal-Wallis H rank sum test (**a**), Spearman correlation analysis (two-tailed) (**b–e**), unpaired two-tailed Student's *t* test (**f**, **l**, **n**, **p–s**), two-tailed Mann-Whitney test (**g**, **k**), two-way ANOVA repeated-measure with Sidak's multiple comparisons test (**j**, **m**, **o**) and exact *P* value were shown in figure panels. Source data are provided in a Source data file.

expression levels (Supplementary Fig. 13e). These results indicate that disruption to the gut microbiota can affect the levels of *Slc2a4* in the liver and thus influencing the obesity phenotype.

Furthermore, FMT from 80% LRD mice to HFD recipients elevated liver *Slc2a4* mRNA (Fig. 5d), indicating microbiota-mediated regulation. Oral supplementation with *P. goldsteinii* or MIAA similarly

increased liver *Slc2a4* expression in HFD mice (Fig. 5e, f), linking their anti-obesity effects were associated with this pathway. Notably, our encapsulation technology further enhanced *P. goldsteinii*'s induction of *Slc2a4* mRNA (Supplementary Fig. 13f). Consistent with this, when we used an MIAA intervention on an insulin-resistant cell models, we also observed the restoration of *Slc2a4* mRNA expression levels (Fig. 5g

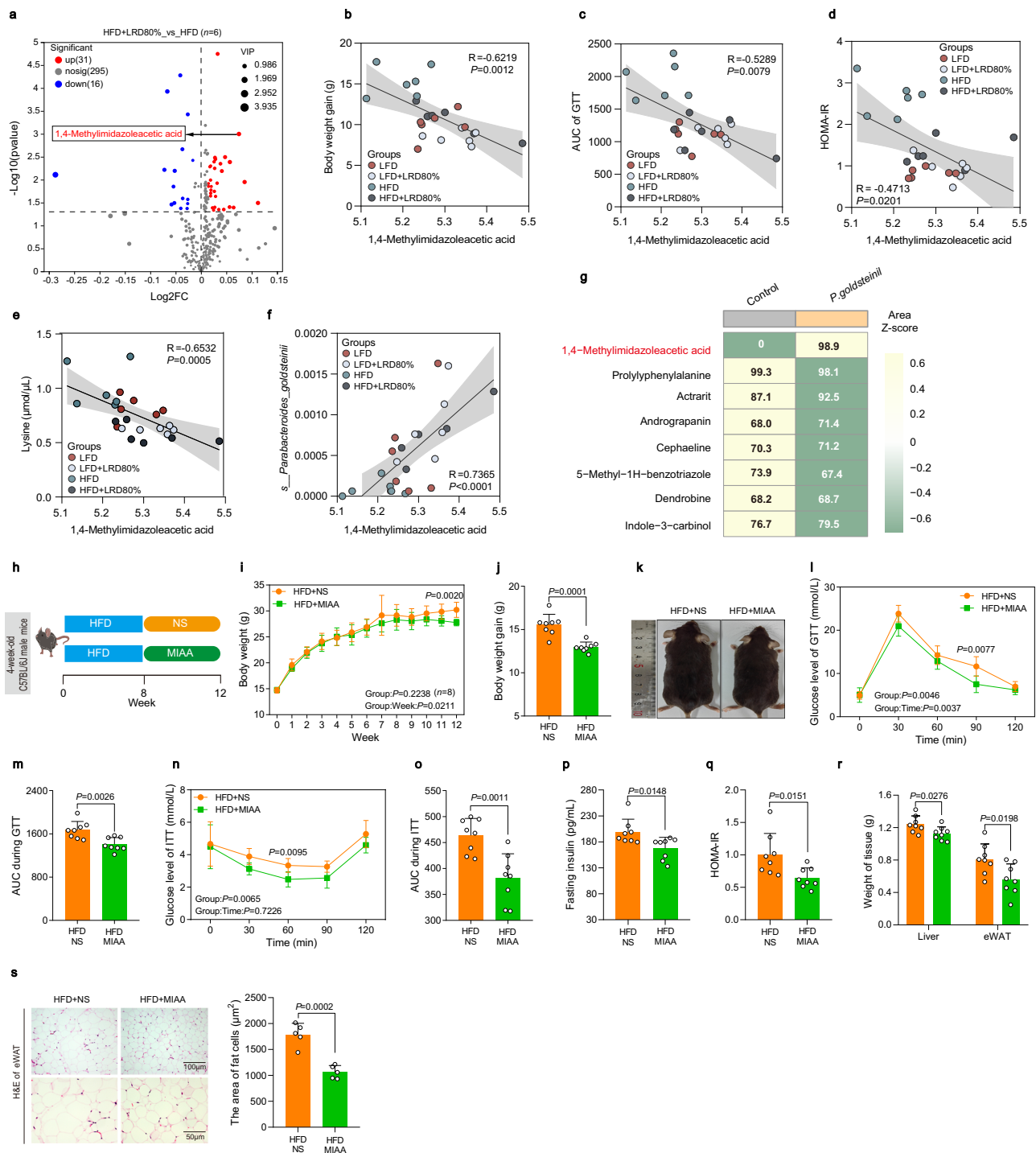


Fig. 4 | *P. goldsteinii* may exert anti-obesity benefits through MIAA. **a** Volcano plot of differential metabolites based on fold change and *P*-values (red dots are metabolites with $\text{Log}_2\text{FC} > 1$, $P < 0.05$, blue dots are metabolites with $\text{Log}_2\text{FC} < -1$, $P < 0.05$, and grey dots are metabolites with $|\text{Log}_2\text{FC}| < 1$, $P > 0.05$). **b–f** Correlation of 1,4-methylimidazoleacetic acid concentration with body weight gain, AUC of GTT, HOMA-IR, lysine and *P. goldsteinii* in mice and linear regression lines with 95% confidence intervals. **g** Identification of material in *P. goldsteinii* culture and blank medium based on LC-MS. **h** Flow chart of the animal experiments. **i, j** The body weight and body weight gain of mice in each group over the course of the 12-week experiment. **k** Differences in body size of mice between different groups after 12 weeks of treatment. **l–q** Glucose metabolism of mice in each group at the end of experiment including GTT with AUC (**l, m**), ITT with AUC (**n, o**), fasting insulin (**p**)

and HOMA-IR (**q**). **r** The weights of liver and eWAT of mice from each group after the 12-week experiment. **s** Pathological changes in the liver and eWAT of mice exposed to different treatments for 12 weeks, including H&E stained sections (representative images) (scale bars, 50 μm and 100 μm) and the area of fat cells. Each dot represents a metabolite (**a**). Each point in graphs (**b–f, i, m, o–r**) represents the value obtained in an independent mouse ($n = 6$ or 8 per group). Data were presented as mean ± S.E.M. *P* values were calculated with the unpaired two-tailed Student's *t* test (**a, j, m, o, q–s**), *Person* correlation analysis (two-tailed) (**b**), *Spearman* correlation analysis (two-tailed) (**c–f**), two-way ANOVA repeated-measure with Sidak's multiple comparisons test (**i, l, m**), two-tailed Mann-Whitney test (**p**) and exact *P* value were shown in figure panels. Source data are provided in a Source data file.

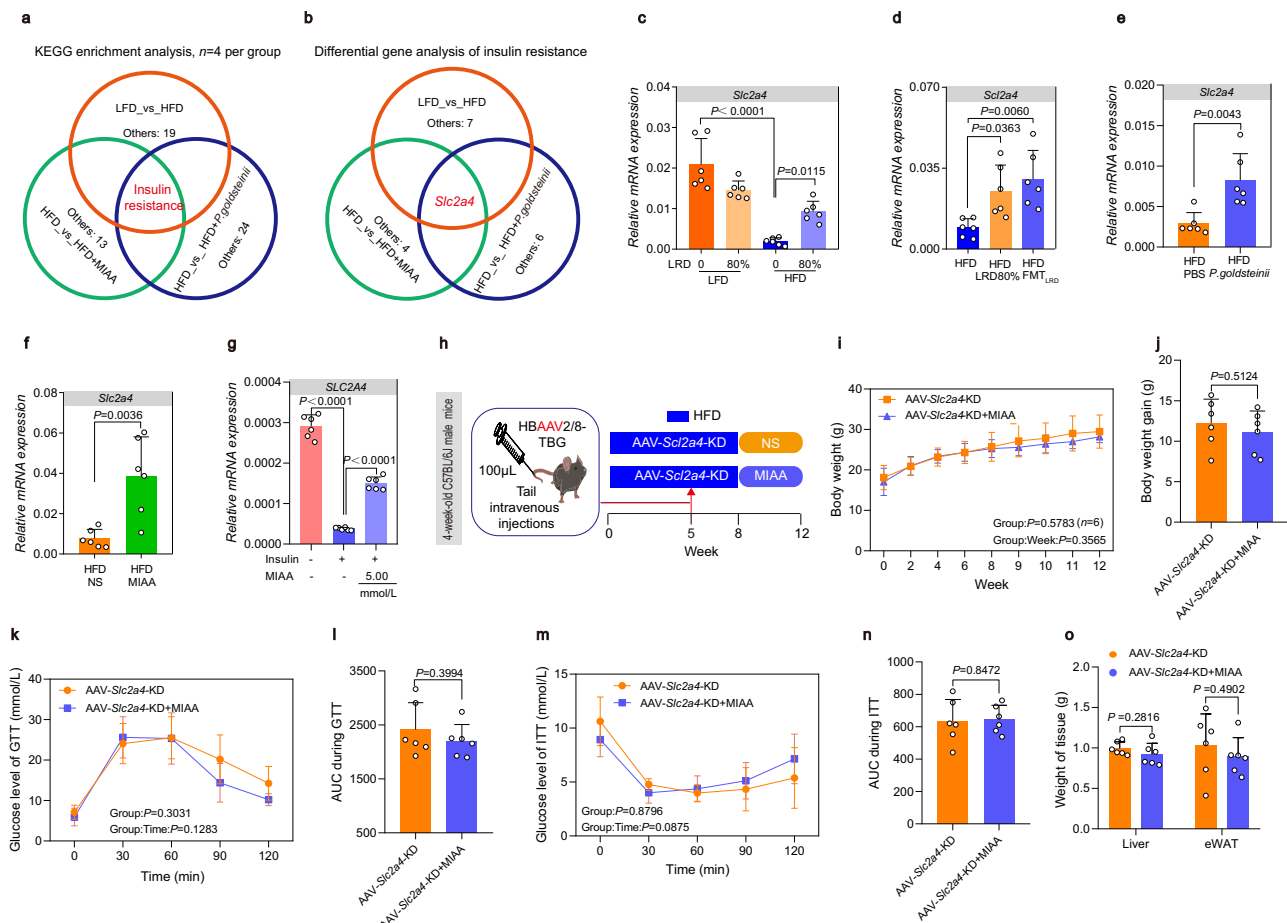


Fig. 5 | MIAA exerts anti-obesity effects by upregulating *Slc2a4*. **a** Venn plots showing the results of KEGG enrichment analysis from three experiments ($n = 4$ per group). **b** Venn plots showing the results of differential gene analysis of insulin resistance from three experiments ($n = 4$ per group). **c** The mRNA expression level of *Slc2a4* in liver of mice after 8 weeks of dietary interventions. **d** The mRNA expression level of *Slc2a4* in liver of mice after 12 weeks of exposure to HFD, HFD + LRD80% and HFD + FMT_{LRD80%}. **e** The mRNA expression level of *Slc2a4* in liver of mice after 12 weeks of exposure to HFD + PBS and HFD + *P. goldsteinii*. **f** The mRNA expression levels of *Slc2a4* in liver of mice after 12 weeks of exposure to HFD + NS and HFD + MIAA. **g** The expression levels of *SLC2A4* mRNA in the cells after treated with MIAA for 24 hours in the insulin-resistant THLE-2 cell model.

h Flow chart of the animal experiments. **i, j** The body weight and body weight gain of mice in each group over the course of the 12-week experiment. **k–n** Glucose metabolism of mice in each group at the end of experiment including GTT with AUC and ITT with AUC. **o** The weights of liver and eWAT of mice. Each circle represents an independent experiment (**a**). Each point in graphs (**c–f, j, l, n, o**) represents the value obtained in an independent mouse ($n = 6$ per group). Data were presented as mean \pm S.E.M. P values were calculated with the one-way ANOVA followed by Tukey's *post-hoc* analysis (**c, d, g**), two-tailed Mann-Whitney test (**e**), unpaired two-tailed Student's *t* test (**f, j, l, n, o**), two-way ANOVA repeated-measure with Sidak's multiple comparisons test (**i, k, m**) and exact P value were shown in figure panels. Source data are provided in a Source data file.

and Supplementary Fig. 14g). These results suggest that *Slc2a4* may mediate the anti-obesity effects of *P. goldsteinii* and MIAA.

Subsequently, we knocked down the expression of *Slc2a4* in mouse liver tissue using an adeno-associated virus (AAV), and the knock-down efficiency was validated (Supplementary Fig. 13h–j). We found that, after KD of *Slc2a4*, the anti-obesity effect of MIAA was significantly attenuated, as evidenced primarily by the cessation of weight loss and the stronger of systemic insulin resistance effects (Fig. 5h–o). Additionally, employing a strategy of three intraperitoneal injections of the *Slc2a4* protein inhibitor fasentin, we found that this treatment attenuated the ameliorative effects of MIAA on the obese phenotype in HFD-fed mice (Supplementary Fig. 13k–s).

MIAA enhances *Slc2a4* through FTO-mediated m⁶A modification to exert anti-obesity effects

To clarify whether the increase in *Slc2a4* expression was related to m⁶A modification, we first validated whether there was a significant decrease in m⁶A modification levels on *Slc2a4* mRNA in an in vitro model (Fig. 6a). Dot blot analysis confirmed that total m⁶A modification levels in the liver tissue significantly increased after LRD in two

mouse models of obesity (Fig. 6b and Supplementary Fig. 14a), and this was primarily associated with decreased FTO expression, while the expression levels of other m⁶A methyltransferases and demethylases did not significantly change (Fig. 6c and Supplementary Fig. 14b–f). Within the in vitro insulin-resistant cellular model, we observed a reduction in the level of intracellular m⁶A modifications (Fig. 6d and Supplementary Fig. 14g). Importantly, we observed significant changes in the expression levels of *Fto* mRNA and protein in the liver tissue of HFD mice after fecal transplantation (Fig. 6e and Supplementary Fig. 14h), *P. goldsteinii* treatment (Fig. 6f and Supplementary Fig. 14i), and MIAA treatment (Fig. 6g). Consistent with these observations, MIAA treatment also normalized the increase in FTO levels and the changes in m⁶A modification levels, as observed in the cell model (Fig. 6h, i). Next, to verify whether FTO affects obesity by altering the expression levels of *Slc2a4*, we used AAV to construct mice with liver-specific *Fto* KD (Supplementary Fig. 14j–l). It was found that the intervention effect of MIAA on HFD mice was inhibited (Fig. 6j–q). Further, we also constructed transgenic mice with systemic *Fto* KD. The results showed that systemic *Fto* KD abolished the anti-obesity effects of *P. goldsteinii* and MIAA (Fig. 7a–p).

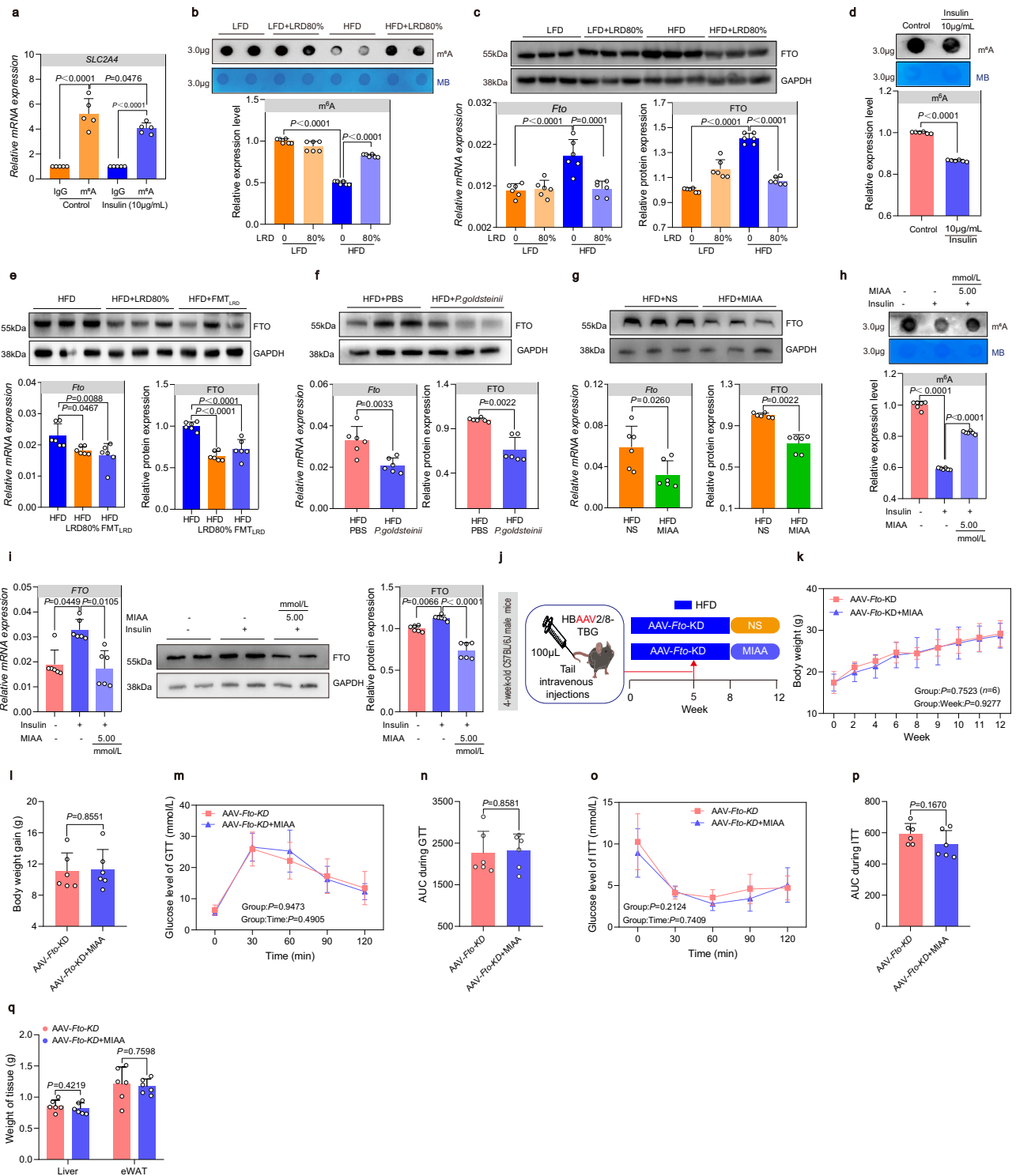


Fig. 6 | MIAA regulates *Slc2a4* expression through *FTO*-mediated m⁶A modification to exert anti-obesity effects. **a** RIP-qPCR was used to detect the degree of m⁶A modification on *SLC2A4* mRNA in THLE-2 cells. **b** Top: representative blots. Under: Dot blot analysis of m⁶A modification levels of total RNA in mice ($n = 2$ per group). **c** Top: representative blots. Bottom left: mRNA expression of *Fto* in the indicated mice. Bottom right: *Fto* expression in liver ($n = 3$ or 6 per group). **d** Top: representative blots. Under: Dot blot analysis of m⁶A modification levels of total RNA in THLE-2 cells after 48 hours of 10 μg/mL insulin treatment. **e** Top: representative blots. Bottom left: mRNA expression of *Fto* in indicated mice. Bottom right: *Fto* expression in liver ($n = 3$ or 6 per group). **f** Top: representative blots. Bottom left: mRNA expression of *Fto* in the indicated mice. Bottom right: *Fto* expression in liver ($n = 3$ or 6 per group). **g** Top: representative blots. Bottom left: mRNA expression of *Fto* in the indicated mice. Bottom right: *Fto* expression in liver ($n = 3$ or 6 per group). **h** Top: representative blots. Under: Dot blot analysis of m⁶A modification levels of total RNA in the insulin-resistant (IR) THLE-2 cell model after treatment with MIAA for 24 hours. **i** Left: mRNA expression of *Fto*. Middle: representative blots. Right: *Fto* expression in the IR THLE-2 cell model after being treated with MIAA for 24 hours. **j** Flow chart of the animal experiments. **k**, **l** Body weight and body weight gain of mice in each group. **m**–**p** Glucose metabolism of mice in each group including GTT, AUC of GTT, ITT and AUC of ITT. **q** Weights of liver and eWAT of mice. Each point in graphs (**l**, **n**, **p**, **q**) represents the value obtained in an independent mouse ($n = 6$). Data were presented as mean ± S.E.M. *P* values were calculated with the one-way ANOVA followed by Tukey’s *post-hoc* analysis (**a**–**c**, **e**, **h**, **i**), unpaired two-tailed Student’s *t* test (**d**, **l**, **n**, **p**, **q**), two tailed Mann-Whitney test (**f**, **g**), two-way ANOVA repeated-measure (**k**, **m**, **o**) and exact *P* value were shown in figure panels. Source data are provided in a Source data file.

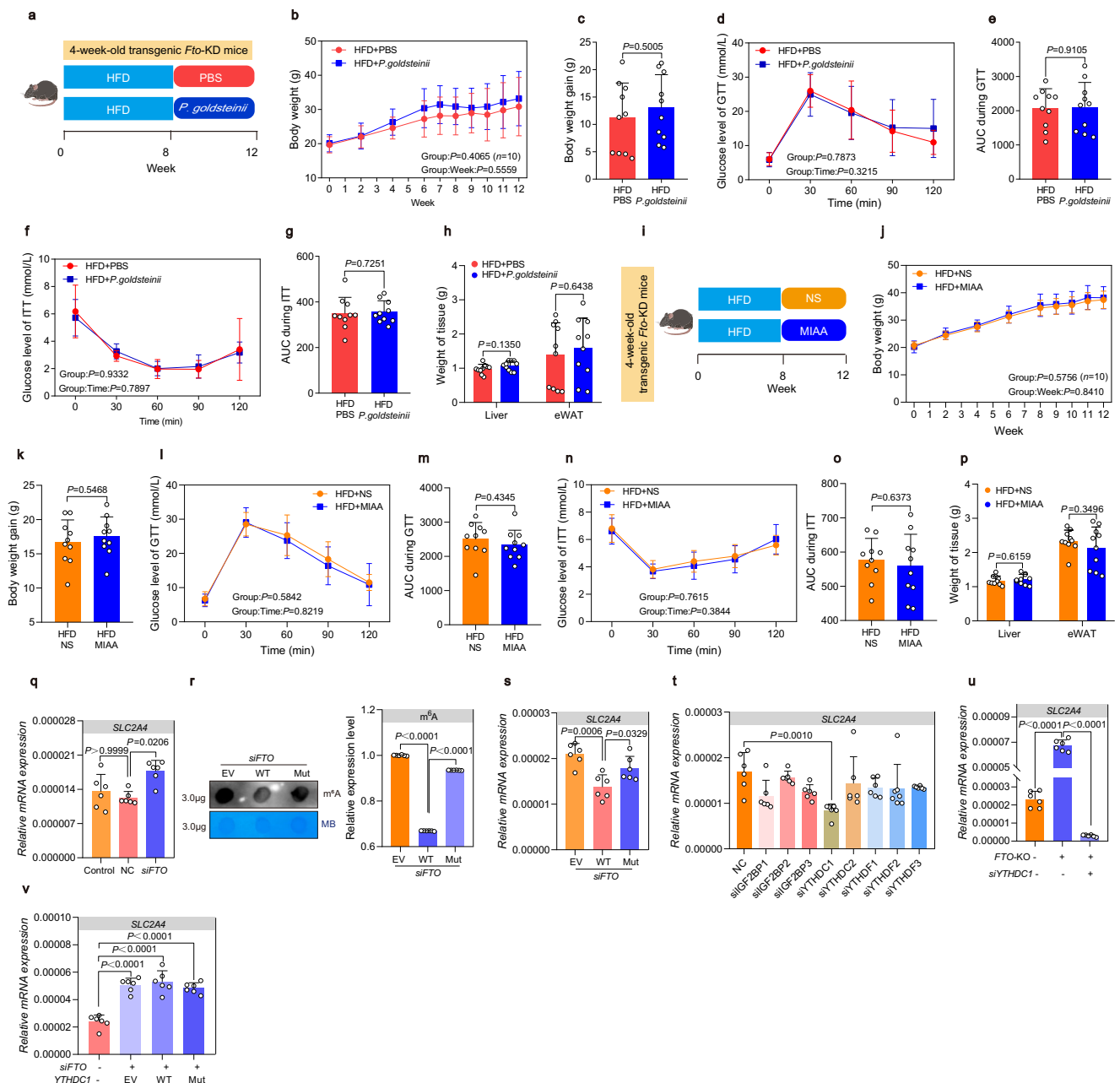


Fig. 7 | FTO/YTHDC1 axis regulates m⁶A modification of SLC24A4. **a** Flow chart of the animal experiments. **b, c** The body weight and body weight gain of mice in each group after 4 weeks of exposure *P. goldsteinii* in *Fto*-KD mice. **d–g** Glucose metabolism of mice in each group at the end of experiment including GTT with AUC, and ITT with AUC. **h** The weights of liver and eWAT of mice from each group. **i** Flow chart of the animal experiments. **j, k** The body weight and body weight gain of mice in each group after 4 weeks of exposure MIAA in *Fto*-KD mice. **l–o** Glucose metabolism of mice in each group at the end of experiment including GTT with AUC, and ITT with AUC. **p** The weights of liver and eWAT of mice from each group. **q** The expression levels of *SLC24A4* mRNA in THLE-2 cells after inhibiting *FTO* mRNA by siRNA. **r** Left: representative blots. Right: Dot blot analysis of m⁶A modification level of total RNA in THLE-2 cells transfected with different plasmids of *siFTO*. **s** The expression levels of *SLC24A4* mRNA in THLE-2 cells transfected with different

plasmids of *siFTO*. **t** The expression level of *SLC24A4* mRNA in insulin-resistant THLE-2 cells after inhibiting m⁶A reader mRNA by siRNA. **u** After knocking down *FTO* through CRISPR-Cas9 technology, the expression levels of *SLC24A4* mRNA in THLE-2 cells with or without *YTHDC1* mRNA inhibited. **v** The expression levels of *SLC24A4* mRNA in THLE-2 cells transfected with different plasmids of *YTHDC1* after inhibiting *FTO* mRNA by siRNA. Each point in graphs (**c, e, g, h, k, m, o, p**) represents the value obtained in an independent mouse ($n = 10$ per group). Data were presented as mean \pm S.E.M. *P* values were calculated with the two-way ANOVA repeated-measure (**b, d, f, j, l, n**), unpaired two-tailed Student's *t* test (**c, e, g, h, k, m, o, p**), Kruskal-Wallis test followed by Dunn's *post-hoc* analysis (**q, t**), one-way ANOVA followed by Tukey's *post-hoc* analysis (**r, s, u, v**) and exact *P* value were shown in figure panels. Source data are provided in a Source data file.

Next, to confirm whether *FTO* regulates the abundance of *Slc2a4* in an m⁶A-modification-dependent manner, we constructed a plasmid with the *FTO* gene mutated (or not) at the m⁶A modification site. To verify the results, we conducted the following in vitro experiments using cell line. After transfection with small interfering RNA targeting *FTO* (*siFTO*), we found that the expression level of *SLC24A4* mRNA was

elevated (Fig. 7q and Supplementary Fig. 15a). *FTO* wildtype and *FTO* mutant plasmid expression was silenced. The results showed that the *FTO* mutant plasmid did not affect m⁶A modification or *FTO* expression (Fig. 7r and Supplementary Fig. 15b), and silencing the *FTO* mutant plasmid did not significantly downregulate the expression level of *SLC24A4* mRNA (Fig. 7s). These results indicate that *FTO* regulates the

expression level of *SLC2A4* mRNA through m⁶A modification. m⁶A modification usually requires the participation of reader proteins (Supplementary Fig. 15c). Therefore, we next used siRNA technology to clarify YTHDC1 was the key specific m⁶A-reading protein under non-stimulation conditions (Fig. 7t).

To confirm whether FTO regulates the expression level of *SLC2A4* mRNA in an m⁶A-modification-dependent manner by recruiting YTHDC1 (Supplementary Fig. 15d, e), we further constructed stable *FTO* KO cells (Supplementary Fig. 15f). After transfection of *FTO* KO cells with si*YTHDC1*, we found that the expression level of *SLC2A4* mRNA was reduced (Fig. 7u). To confirm whether YTHDC1 mediated the regulation the expression level of *SLC2A4* mRNA in an m⁶A-modification-dependent manner, we constructed a plasmid with mutations at the YTHDC1 modification site. After transfection with si*FTO*, the YTHDC1 wildtype or YTHDC1 mutant plasmids were silenced. The results showed that the YTHDC1 mutant plasmid significantly inhibited the regulatory effect of *SLC2A4* (Fig. 7v). These results indicate that FTO regulates the expression level of *SLC2A4* mRNA through YTHDC1-mediated m⁶A modifications.

Discussion

We first demonstrate that LRD may effectively ameliorate childhood obesity. While conventional obesity management is often limited by safety concerns and irreversible effects-reserved for severe cases^{38–40}. The WHO advocates lifestyle modifications such as improved diet quality and reduced caloric intake⁵. This study revealed elevated serum lysine levels in children with obesity, which is consistent with adult data⁴¹, indicating that lysine levels were associated with obesity independent of age. LRD induced significant weight loss in two animal models, indicating efficacy regardless of genetic background or intervention pattern. Critically, LRD caused no malnutrition or metabolic abnormalities in LFD/HFD mice. LRD reduced HFD mouse weight and improved phenotypes comparably to orlistat, but without synergistic effects. Unlike pharmacotherapy, LRD offers safer, more economical, and widely applicable prospects. Importantly, this study confirmed the response of the intestinal microbiota to LRD and its crucial role in the anti-obesity effect of LRD. We also used sequencing methods to screen and verify the anti-obesity effects of LRD by affecting a key emerging probiotic, *P. goldsteinii*. This weight loss effect was mainly attributed to *P. goldsteinii*'s ability to enhance the level of MIAA and activate the *FTO*–*YTHDC1*–*SLC2A4* axis in an m⁶A-dependent manner, thereby increasing insulin resistance levels and ultimately alleviating the phenotype of obesity (Fig. 8).

The prevailing consensus suggests that the microbiota is a key factor influencing obesity^{20,42}, and researchers have attempted to utilize FMT as a method for weight loss in clinical trials⁴³. We used ABX-treated mice to model post-dietary microbial recovery—a more physiologically relevant approach than germ-free (GF) mice^{44,45}, whose complete sterility rarely occurs naturally. FMT from children with obesity induced metabolic dysfunction in LFD mice, whereas FMT from healthy children improved obesity in HFD mice. This childhood-FMT strategy enhances human relevance in obesity research. Furthermore, FMT from LRD HFD mice into ABX-treated HFD recipients conferred metabolic benefits.

However, we should maintain a certain level of caution regarding this approach. The efficacy of FMT can be influenced by various factors, including donor source, recipient status, and environmental conditions⁴⁶. Moreover, although some bacteria are known to be beneficial for weight loss, FMT procedures cannot exclude certain potentially obesogenic bacteria that may promote or exacerbate obesity phenotypes. Therefore, studies are now gradually starting to seek out core anti-obesity probiotic species with high abundance^{47,48}. Based on this new concept, this study analyzed 16S rRNA gene sequencing results from a mouse model of LRD and identified, screened, and verified the role of an anti-obesity bacterium,

P. goldsteinii. Previous animal and clinical studies have consistently reported that obesity is often accompanied by a certain inflammatory state that can lead to a continuous decrease in the abundance of Parabacteroides species^{49,50}. In this study, we found that *P. goldsteinii* was the only significantly decreased species within the Parabacteroides genus after HFD induction, and its abundance significantly increased after LRD intervention. This increase was closely correlated with insulin resistance coefficients and lysine levels. Moreover, in vivo experiments, *P. goldsteinii* also demonstrated a strong anti-obesity effect, making it a potential candidate for next-generation probiotics targeting obesity.

As a core gut commensal, *P. goldsteinii* influences metabolic diseases via gut-bidirectional interactions⁵¹. It enhances intestinal barrier integrity and reduces inflammation, improving microbiota function⁵². We confirmed its barrier-repair capacity in obese mice and developed gastric-resistant encapsulation to promote intestinal colonization, enhancing anti-obesity efficacy. The carbohydrate breakdown products of Parabacteroides species include acetic acid and succinate⁵³, and *P. goldsteinii* was recently reported to produce 7-keto-lithocholic acid, which could also alleviate intestinal barrier damage⁵². Coincidentally, we identified in LRD-intervention mouse plasma and *P. goldsteinii* cultures. Gavage of MIAA reduced weight and insulin resistance in HFD mice, establishing a new mechanism: *P. goldsteinii* ameliorates obesity via MIAA production. This expands known *P. goldsteinii* metabolites, being the first report of its obesity regulation through acetic-acid-like compounds. Consistent results in juvenile and adult mouse models, alongside childhood microbiota usage, suggest translational potential for the LRD-*P. goldsteinii* axis despite species limitations.

We identified *Slc2a4* as a key target gene mediating MIAA's action. As one of the 14 members of the SLC2A family, *Slc2a4* serves as the primary mediator of glucose clearance from circulation and a critical regulator of whole-body glucose homeostasis⁵⁴. Notably, the protein encoded by *SLC2A4* expression levels have been shown to be selectively reduced in obesity and type 2 diabetes patients⁵⁵. Our results also demonstrate that MIAA has a significant promoting effect on *Slc2a4* mRNA expression. This promotion further enhances cellular glucose uptake and metabolic function, leading to decreased blood glucose levels and the alleviation of insulin resistance effects⁵⁶. Recent studies have confirmed the significant role of human ALKB homolog 5 (ALKBH5) in regulating the m⁶A demethylation of *Slc2a4* mRNA and, therefore, the regulation of glycolytic function in drug-resistant breast cancer cells⁵⁷. However, the mechanism by which *Slc2a4* regulates m⁶A modifications is not fully understood. Building upon this foundation and based on our results, we propose a new potential mechanism: the impact of *Slc2a4* on insulin resistance may be achieved through an FTO-mediated m⁶A-modification-dependent pathway. Considering the presence of the two m⁶A demethylases, FTO and ALKBH5, which may have simultaneous roles in removing m⁶A modifications, our study findings imply that specific FTO-mediated m⁶A modification of *Slc2a4* occurs through the non-differential expression of the ALKBH5 protein.

Importantly, our results also confirmed that, after LRD intervention, the expression levels of FTO decreased in liver tissue, consistent with the simultaneous production of anti-obesity effects. This mechanism may be attributed to two factors: First, the decrease in FTO expression can lead to an increase in m⁶A modifications on *Slc2a4* mRNA, enhancing *Slc2a4* mRNA expression, alleviating insulin resistance, and thus improving the obesity phenotype. Second, besides being a m⁶A demethylase significantly altered in obesity models, FTO is also a protein closely associated with obesity³⁸. Therefore, inhibiting FTO may directly contribute to weight loss effects. However, in our in vitro cell experiments, we found that mutating the m⁶A demethylase

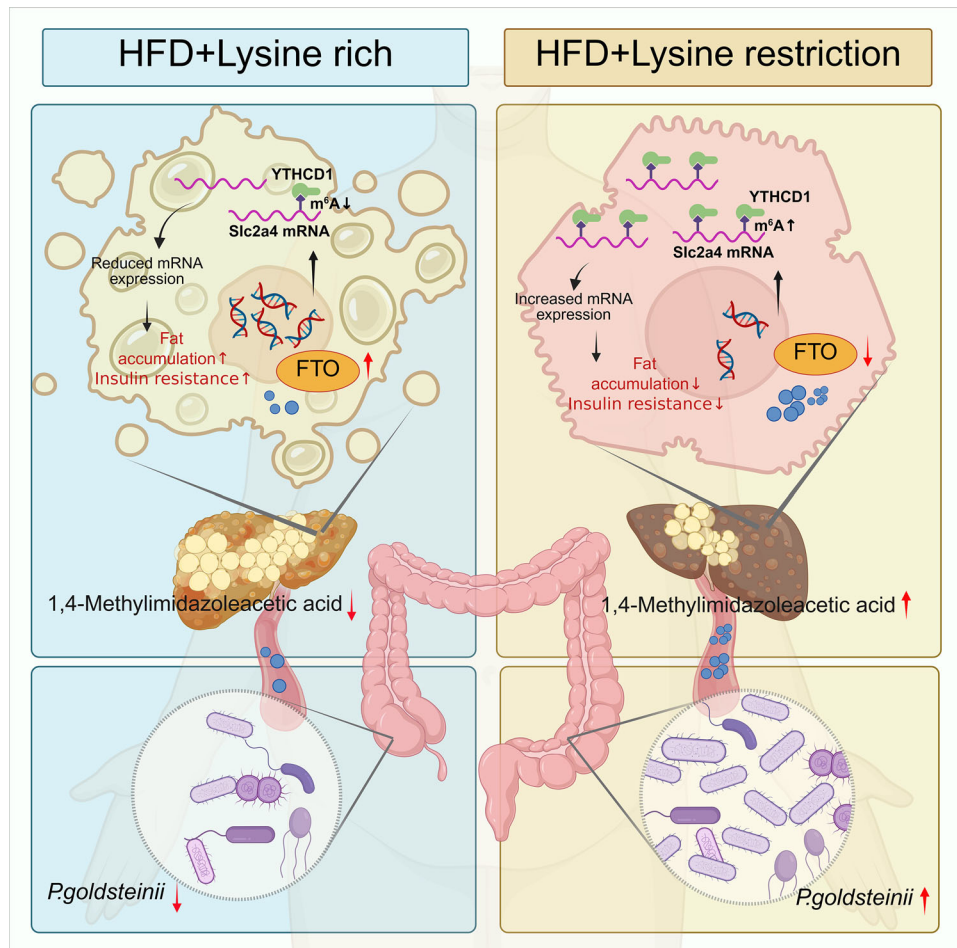


Fig. 8 | Schematic model of the mechanism underlying LRD-induced obesity reduction. LRD enriches *P. goldsteinii*, which produces MIAA to reduce adiposity. This effect is potentially mediated via upregulation of the FTO-YTHDC1-SLC2A4 axis, leading to inhibition of adipose tissue expansion. Created by Biorender.

activity site of FTO achieved effects similar to those of FTO knockdown in terms of weakening insulin resistance. This suggests that the regulatory mechanism of FTO's effect on obesity may be more complex and involve various regulatory pathways, such as FTO-mediated m⁶A modification in liver/adipocyte cells⁵⁹ and the coexistence of FTO single-nucleotide polymorphisms⁶⁰. Furthermore, the biological regulation of m⁶A modification generally requires the involvement of m⁶A reader proteins⁶¹. This study also screened and identified YTHDC1 as the key reader protein regulated by FTO in the control of *Slc2a4* stabilization and confirmed that YTHDC1 can bind to m⁶A modifications on, and thereby stabilize the *Slc2a4* mRNA, contributing to its increased abundance.

Interestingly, our study identified *Slc2a4* as the only differentially expressed gene in the altered insulin resistance signaling pathway in the liver under LRD and gut microbiota modulation. While *Slc2a4* is typically expressed in adipose tissue and skeletal muscle⁵⁴, its upregulation in the liver suggested a novel, non-canonical role that may be critical in specific metabolic contexts. This atypical expression might be driven by the unique metabolic environment induced by LRD, potentially mediated by gut microbiota-derived metabolites like MIAA. MIAA's modulation of m⁶A levels in *Slc2a4* mRNA and inhibition of FTO-mediated YTHDC1 supported the idea that genes with weak liver expression can become functionally significant under altered conditions. Although the precise mechanisms require further investigation, our findings suggest an unrecognized role for *Slc2a4* in liver metabolism. Future studies should explore this role, focusing on its regulatory

mechanisms and implications in disorders like obesity and insulin resistance.

Three limitations have to be addressed. First, the use of maltosaccharin as an isocaloric substitute for lysine-calories in diets, while necessary to maintain caloric parity across groups, introduces potential confounding due to divergent metabolic pathways between oligosaccharides and amino acids^{62,63}. Although maltosaccharin demonstrates metabolic neutrality in glycemic/insulin responses⁶⁴, future studies should incorporate gut microbiota profiling and alternative substitution strategies. Second, while our protocol minimized exposure duration, we acknowledge that glycerol may still enrich osmotic-tolerant bacterial species^{52,65}, potentially causing minor community structure changes. Third, while the human-origin *P. goldsteinii* strain (JCM: 13446T) enhances clinical relevance⁶⁶, host-specific evolutionary adaptations in murine versus human strains may exist. Whole-genome sequencing and host-microbe interaction studies are required to validate functional equivalence across host species.

In summary, our study has provided preliminary evidence demonstrating that gut microbiota that thrive under an LRD, specifically *P. goldsteinii*, have the ability to enhance MIAA. This compound activated the FTO-YTHDC1-SLC2A4 axis, consequently lowering insulin resistance levels and ultimately ameliorating the phenotype of obese mice. These findings not only emphasize the pivotal role of gut microbiota in children with obesity but also offer novel insights and ideas relating to innovative therapeutic intervention strategies.

Methods

We provide a list of key resources used in this study in Supplementary Table 2.

Human subjects

This research included 30 children with obesity aged between 6 and 12 and 30 healthy controls to compare plasma free lysine levels. Inclusion criteria: the obesity group was verified to have primary obesity; controls were not obese. Both groups excluded recent infections, surgery, antibiotic use (1 month), and congenital/genetic diseases. Of the 263 initially screened, 60 participants were selected via strict screening (Supplementary Fig. 16); all participants and their guardians provided written informed consent. Data were anonymized using unique codes. The investigators were blinded to group allocation during data collection and/or analysis. Chongqing Medical University's Ethics Committee (No.2023003) approved the study in accordance with the Helsinki Declaration. Only aggregated findings were presented.

Experimental animals

This study used 4-week-old C57BL/6J (male/female), 6-week-old male *Leptin*-KO, and 4-week-old male *FTO* heterozygous transgenic mice. The mice were sourced from Chongqing Medical University [license SYXK (Chongqing) 2022-0016], Jiangsu GemPharmatech Co., Ltd [license number: SCXK(Su)2023-0009], and Chengdu GemPharmatech Co., Ltd [license numbers: SCXK(Chuan) 2020-0034]. All mice were housed under specific pathogen-free (SPF) conditions, with controlled room temperature ($23 \pm 1^\circ\text{C}$), humidity ($50\% \pm 10\%$), and a 12 h/12 h light/dark cycle. Food and water were provided ad libitum. The study protocol was approved by the Chongqing Medical University Ethics Committee (IACUC-CQMU-2023-0465). Animals were subjected to stratified randomization based on body weight, using computer-generated random numbers from www.random.org. To further mitigate potential confounding factors, processing order and measurement sequences were randomized throughout the experimental procedures and data collection. Blinding protocols were used throughout group allocation, experimental execution, result evaluation, and data processing to ensure scientific integrity.

Cell culture

The Human THLE-2 cell line (CL-0833, Pricella) was obtained from ATCC and cultured in specific medium (CM-0833, Pricella) at 37°C with 5% CO_2 . HEK293T (CL-0005) was maintained in DMEM (A1451801, Thermo Fisher) supplemented with 10% fetal calf serum (S711-001S, Lonsera), 100 U/mL penicillin/streptomycin (15140122, Gibco). The cells were collected at 80% confluence for experiments.

Bacterial culture conditions and encapsulation

P. goldsteinii (13446, JCM) was anaerobically cultured in GAM broth/agar (Supplementary Table 3) supplemented with 0.1% vitamin K1 and hemin at 37°C (80% N_2 /10% CO_2 /10% H_2), all procedures performed inside in an anaerobic chamber. To enhance gastric resistance and intestinal colonization, we developed a three-layer encapsulation: outer gum Arabic, middle chitosan, and inner alginate-embedded bacterial suspension, adapted from previous methods⁶⁷.

Lysine-restricted diet (LRD) intervention in the obesity model mice

Lysine-restricted diets (LRD: 40% or 80% lysine reduction) were formulated by replacing lysine calories with isocaloric maltosaccharin in low-fat (LFD, 10% fat) or high-fat diets (HFD, 60% fat) (Supplementary Table 4). Three experiments were conducted: the Obesity model: 96 male C57BL/6J mice (4-week-old) received an HFD/LFD + LRD for 8 weeks (weight/blood glucose was monitored at 4/8 weeks). *Leptin*-KO validation: 16 male *Leptin*-KO mice (6-week-old) were fed LFD or LFD + LRD80% for 6 weeks. Drug comparison: 32 male C57BL/6J mice

(4-week-old) received HFD or HFD + LRD80% for 8 weeks, followed by 14-days of treatment with orlistat (10 mg/kg/day) vs saline control.

Fecal microbiota transplantation (FMT)

Human-animal FMT was performed under anaerobic conditions. Pooled fecal samples from children with obesity and healthy controls (200 mg each) were homogenized in PBS, centrifuged ($200 \times g$, 4°C), washed, and resuspended in 20% glycerol-PBS (sterile equipment). A total of 32 four-week-old male C57BL/6J mice received LFD/HFD for 8 weeks, followed by pretreatment with 200 μL of antibiotic cocktail (ABX) (Supplementary Table 5) for 14 days. ABX-treated mice were gavaged with 200 μL daily of the following: (1) children with obesity microbiota suspension (LFD group), (2) healthy control microbiota suspension (HFD group), or (3) PBS controls.

For microbiota-dependent anti-obesity validation, 24 mice (4-week-old) were divided: 16 received HFD for 8 weeks + ABX, while 8 received HFD + LRD80%. Fecal suspensions from HFD + LRD80% mice were transplanted into HFD-fed mice using the above protocol. All procedures were performed under strict anaerobic conditions and were adapted from previous protocols.

Effects of *P. goldsteinii* and MIAA supplementation on male mice fed an HFD

Male C57BL/6J mice (4-week-old, $n = 32$) received HFD for 8 weeks, followed by daily oral gavage of either: (1) active *P. goldsteinii* (200 μL , 1×10^9 CFU/mL) or MIAA (50 mg/kg), or (2) vehicle control for 28 days while maintaining HFD.

Effects of supplementation with inactivated *P. goldsteinii* on male mice fed an HFD

Male C57BL/6J mice (6-week-old, $n = 22$) were fed an HFD for 8 weeks. While the HFD was continued, the mice subsequently received daily oral gavage of either inactivated *P. goldsteinii* (200 μL , 1×10^9 CFU/mL) or the vehicle control for 28 days.

Effects of *P. goldsteinii* and MIAA supplementation on female mice fed an HFD

Female C57BL/6J mice (4-week-old, $n = 34$) received HFD for 8 weeks, followed by daily oral gavage of either: (1) active *P. goldsteinii* (200 μL , 1×10^9 CFU/mL) or MIAA (50 mg/kg), or (2) vehicle control for 28 days while maintaining HFD.

P. goldsteinii supplementation for metabolic abnormalities in Young Mice

Male C57BL/6J ($n = 16$, 4-week-old) and *Leptin*-KO mice ($n = 18$, 4-week-old) underwent HFD (2 weeks) or LFD (1 week) acclimation, respectively, followed by daily oral gavage of 200 μL active *P. goldsteinii* (1×10^9 CFU/mL) or vehicle control for 28 days.

Simulated gastric fluid (SGF) and simulated intestinal fluid (SIF)

Simulated gastrointestinal resistance: Microcapsules (1g) were incubated in SGF (0–3 h sampling) and SIF (0–90 min sampling) at 100 rpm. The samples were washed, lysed, and plated for CFU counting, with unencapsulated bacteria used as controls.

Viability assessment: Bacterial suspensions (untreated/SGF-90 min/SIF-3 h) and microcapsules were stained with SYTO9/PI (3 μL dye/mL, 15 min dark incubation). Live/dead bacteria displayed green/red fluorescence, respectively, under microscopy. The microencapsulated groups were subjected to post-staining SGF/SIF treatment before observation, with unstressed encapsulated bacteria used as controls.

Encapsulation of *P. goldsteinii* supplementation to treat obesity

Male C57BL/6J mice (4-week-old, $n = 16$) were fed an HFD for 8 weeks, followed by daily oral gavage of either 200 μL of the active

P. goldsteinii (1×10^9 CFU/mL) or the microencapsulated preparation (200 μ L) for 28 days.

Effects of *P. goldsteinii* and MIAA supplementation on systemic *Fto*-KD mice fed a HFD

Fto-knockdown (KD) mice were produced in accordance with published protocols⁶⁸. Forty male *Fto*-KD mice (4-week-old) received HFD for 8 weeks, followed by daily oral gavage of: *P. goldsteinii* (1×10^9 CFU/mL), MIAA (50 mg/kg) or vehicle control (200 μ L) for 28 days.

Three other animal models of MIAA supplemental intervention
Liver-targeted AAV model: Male C57BL/6J mice (4-week-old, $n = 24$) received tail vein injections of AAV-*Slc2a4/Fto*-KD (100 μ L) or empty vector after 5-week HFD, followed by 8-week HFD maintenance and 28-day MIAA treatment (50 mg/kg/day, oral gavage).

Pharmacological inhibition model: Male C57BL/6J mice ($n = 16$, 4-week-old) were intraperitoneally injected with fasentin (10 mg/kg) on days 1/8/15 post-HFD initiation, maintained on a HFD for 8 weeks, and then administered MIAA (50 mg/kg/day) or vehicle for 28 days.

Metabolic monitoring

For the measurement of energy expenditure, singly housed mice were acclimated to the metabolic chamber of the TSE Phenomaster system for 24 hours at room temperature. O₂ consumption and CO₂ production were monitored and data were collected. Energy expenditure (EE) was calculated as $EE = (3.185 + 1.232 \times VO_2 / VCO_2) \times VO_2$. The respiratory exchange ratio (RER) was calculated as $RER = VCO_2 / VO_2$. Mice were kept in a metabolic chamber at 22 °C for 2 days. The fecal triglyceride content was quantified using enzymatic assays. Samples were incubated (37 °C, 10 min) in 96-well plates, and the absorbance was measured at 500 nm.

Insulin tolerance test and glucose tolerance test

In the glucose tolerance test (GTT), animals were subjected to overnight fasting with access to water, while in the insulin tolerance test (ITT), they were fasted for 6 hours with water available. Fasting blood glucose levels were measured before the intraperitoneal injection of glucose (2.0 g/kg weight) or insulin (0.75 U/kg weight). Blood glucose levels were measured at different time points (0, 30, 60, 90 and 120 min).

Biological sample and tissue collection

Fresh fecal pellets (2–3 per mouse) were collected daily (9:00–10:00 AM) for three days before the conclusion of the dietary intervention and stored at –80 °C. The mice were euthanized via intraperitoneal tribromoethanol (150 mg/kg). Orbital blood was centrifuged (6000 rpm, 4 °C, 10 min), and the plasma was stored at –80 °C. Epididymal white fat tissue (eWAT), the colon, and the liver were dissected and weighed. The samples were fixed in 4% paraformaldehyde (colon/liver) or 10% calcium formaldehyde (eWAT) for >24 h and then flash-frozen in sterile tubes at –80 °C.

Plasma biochemical analysis

Plasma lipid profiles and fasting blood glucose levels were quantified using an automated biochemical analyzer following the manufacturer's protocols.

Insulin level testing

Fasting plasma insulin levels were quantified using species-specific ELISA kits. The human (E-EL-H2665) and mouse (E-EL-M1382c) insulin assays followed identical protocols: samples/standards were incubated (90 min), and treated sequentially with biotinylated antibodies (37 °C, 60 min), HRP conjugates (37 °C, 60 min), and TMB substrate (37 °C, 15 min dark). The reactions were stopped with a stop solution,

and the absorbance was measured at 450 nm. Concentrations were calculated against standard curves.

Homeostatic model assessment of insulin resistance

Homeostatic model assessment of insulin resistance (HOMA-IR) was calculated as $HOMA-IR = (\text{Fasting plasma glucose} \times \text{Fasting insulin}) / 22.5$.

Lysine content detection

The plasma-free lysine content was quantified in human and murine samples using a colorimetric assay (Cell Biolabs, MET-5130). The plasma was incubated with the reaction mixture for 20 min (in the dark), after which the absorbance was measured at 560 nm. Standard curves derived from lysine calibrators enabled concentration determination.

Hematoxylin-eosin(H&E) staining and histopathological analysis

Paraffin-embedded liver, adipose, and colon tissues (5 μ m sections) were stained with H&E using standardized protocols. Colon pathology was assessed blindly by independent evaluators based on specified criteria. Representative images were captured using bright-field microscopy.

RNA extraction and qPCR analysis

Total RNA was extracted from cells or homogenized tissues using TRIzol reagent (Takara, 9109) according to the manufacturer's instructions. The isolated RNA was reverse-transcribed using the cDNA Synthesis Kit (Takara, RRO36A). Quantitative real-time PCR (qPCR) was performed using target-specific primers (Supplementary Table 6) and SYBR Green probes. The reaction conditions for qPCR are provided in Supplementary Table 7. The $2^{-\Delta\Delta Ct}$ method with β -actin as the internal reference control was used to determine the relative mRNA expression level.

Protein extraction and western blotting

Tissue and cell proteins were extracted using RIPA buffer containing protease inhibitors. Protein concentrations were determined by BCA assay (Beyotime, P0009), after which the proteins were denatured (100 °C, 10 min), and separated via SDS-PAGE. The transferred PVDF membranes (LABSELECT, TM-PVDF-R-22) were blocked with 5% skim milk powder, and incubated with primary antibodies 4 °C overnight (see Supplementary Table 8 for details), followed by HRP-conjugated secondary antibodies (1 h, RT). The membranes were then washed three times in TBST (Tris-buffered saline containing 0.1 % Tween 20) before visualization using the New SUPER ECL on a ChemiDoc™ Touch Imaging System. Western blot images were analyzed for densitometry using ImageJ.

RNA extraction and dot blots

Total RNA was extracted (Estep® Super Total RNA Extraction Kit), denatured (95 °C, 3 min), and blotted onto a Nylon Transfer Membrane-N+ membrane (Biosharp, BS-NY-45) using a water circulation multi-functional vacuum pump device (Lichen, SHZ-DIII). The membranes were UV-crosslinked, blocked, incubated with m⁶A antibody, and then incubated with HRP-conjugated secondary antibody (RT/1 h). The signals were detected with New SUPER ECL on a ChemiDoc™ Touch Imaging System. The RNA input was normalized via 0.5% methylene blue staining (Solarbio, G1302).

16S rRNA gene sequencing and data analysis

Fecal DNA was extracted using the PF Mag-Bind Stool Kit (Omega, M4029-00). The V3-V4 region of 16S rRNA was amplified and sequenced on the Illumina PE300 platform according to the standard protocol of Majorbio Bio-Pharm Technology Co. Ltd. Raw reads were

processed with FASTP and FLASH. OTUs were clustered at 97% similarity and taxonomically classified against SILVA v138. Sequence data were rarefied to 34,546 reads/sample. One-way ANOVA for α -diversity. Principal coordinate analysis (PCoA) was used on the basis of the Bray-Curtis distance algorithm to test the similarity of microbial community structures between samples, and was combined with the PERMANOVA non-parametric test to determine whether the differences in microbial community structure between sample groups were significant. Genus and species composition visualization and linear discriminant analysis were performed using R (v4.2.3), and the Kruskal-Wallis test was used for taxonomic differential analysis.

Bacterial DNA extraction and qPCR for 16S ribosomal DNA

Fecal DNA from childhood and murine cohorts was extracted using the TIANamp Stool DNA Kit (TIANGEN, DP328). qPCR amplification with Blast Taq™ 2X qPCR Master Mix (Abm, G891) and target-specific primers (Supplementary table 6) was performed on a Bio-Rad CFX system. The relative bacterial abundance was normalized to that of UMI 16S and calculated via the $2^{-\Delta\Delta Ct}$ method.

Non-targeted metabolomics

Non-targeted metabolomics of mouse plasma (4 groups, 6 samples per group, a total of 24 samples) was conducted utilizing liquid chromatography–tandem mass spectrometry (LC–MS/MS) with a C18 column maintained at 40 °C. The mobile phases consist of (A) 5% acetonitrile/95% water and (B) 47.5% acetonitrile/47.5% isopropanol/5% water, each containing 0.1% formic acid. Data were collected in both positive and negative electrospray ionization modes over a m/z range of 70–1050, utilizing data-dependent acquisition (DDA) with resolutions of 60,000 for MS1 and 7,500 for MS2. The instrument settings included a spray voltage of 3.5 kV, an ion transfer tube temperature of 325 °C, normalized collision energies of 20/40/60 V, and an auxiliary gas temperature of 425 °C. Raw data were processed with Progenesis QI (Waters, UK) for feature detection, alignment, and normalization. Metabolite annotation included correlating precise masses and MS/MS spectra with public databases, including the Human Metabolome Database (HMDB), Metlin, and proprietary reference libraries, supplemented by human verification and quality control measures. To assess analytical reproducibility, pooled quality control (QC) samples, composed from equal aliquots of study plasma, were routinely injected during the run to monitor retention time stability and fluctuations in signal strength. Sample preparation and injection order were randomized among experimental groups, with no significant batch effects identified (Fisher's exact test, $P > 0.05$). After removal of features with missing values and subsequent log₁₀ transformation, the data were subjected to multivariate statistical analysis. Principal component analysis (PCA) and partial least-squares discriminant analysis (PLS–DA) were performed with sevenfold cross-validation. Significantly altered metabolites were defined as those with variable importance in projection (VIP) scores > 1 and a two-tailed Student's t -test P -value < 0.05 . All statistical analyses and data visualization were conducted on the Majorbio Cloud Platform (Shanghai, China).

LC-MS/MS-based substance identification

LC-MS/MS-based metabolite profiling of *P. goldsteinii* supernatant (vs. GAM medium control) was performed using a Sepax GP-C18 column (1.8 μ m, 2.1 \times 150 mm, 40 °C) with mobile phases: 0.1% formic acid (A) and acetonitrile (B); 0.3 mL/min, 21 min). ESI \pm modes were applied. The Raw data (converted to ABF format) were subjected to data-independent MS/MS deconvolution, peak extraction, and alignment in MS-DIAL v4.70, generating a metabolite matrix. Database-matched metabolites were visualized via heatmaps using total identification scores.

RNA sequencing

TRIzol reagent was used for total RNA extraction from liver tissue according to the manufacturer's protocol. RNA-Seq analysis was performed by Major Bio Inc. For RNA-seq analysis, cDNA libraries were constructed with the Illumina Truseq™ RNA sample preparation kit (Illumina, RS–122-2001) using 1 μ g of total RNA. The total RNA was sequenced using the Illumina Novaseq 6000 sequencing System. The expression differences of genes between samples were analyzed using DESeq2, and the screening criteria for significantly differentially expressed genes were FDR < 0.05 and $|\log_2FC| \geq 1$. KOBAS software was used for KEGG annotation, functional classification, and enrichment analysis of differentially expressed genes. The RNA-seq data were deposited in the Gene Expression Omnibus.

Animal adeno-associated virus vector (AAV) construction and virus packaging

AAV vectors (serotype 8) expressing liver-targeted shRNAs against *Slc2a4* or *Fto* under the thyroxine-binding globulin (TBG) promoter were constructed (Hanheng Biological Technology). shRNAs (Supplementary Table 9) were subsequently cloned and inserted into TBG-driven vectors with ZsGreen. Validated plasmids were co-transfected with PAAV-RC and pHelper into 293-AAV cells using Lipofiter™ lipofectamine, followed by 72-h incubation and purification kit (Biomiga, V1469-01). AAVs underwent sterility, mycoplasma, and titer QC. Final titers: *Slc2a4*-shRNA (1.8×10^{12} vg/mL) vs. empty vector (1.7×10^{12}); *Fto*-shRNA (1.7×10^{12}) vs. empty vector (1.8×10^{12}).

Fluorescence staining

Fluorescent nuclear staining was performed on frozen sections using DAPI (Beyotime, C1005). The Sections were thawed at room temperature (30 min), washed three times with PBS, and incubated with DAPI in the dark (3 min). After being washed with PBS, the sections were air-dried, mounted in glycerol, and imaged via fluorescence microscopy.

In vitro experiments with an insulin resistance model

THLE-2 cells were seeded in 96-well plates (1×10^5 cells/well, 100 μ L medium) during log-phase growth. After reaching 80% confluency, cells were treated with insulin (Macklin, I828365) at concentrations of 0, 5, 10, or 20 μ g/mL in culture medium for 24 or 48 h. To establish insulin resistance, cells were subsequently incubated for 48 h in THLE-2-specific maintenance medium (Pricella, CM-0833) containing 10 μ g/mL insulin.

Cell viability test

Cell viability was assessed using MTS reagent (Promega, G3581). Following 1 h incubation (37 °C, 5 %CO₂) with controls, absorbance at 490/630 nm was measured. Cell viability was calculated as $[(OD_{490} - OD_{630}) / (\text{blank mean})] \times 100\%$.

Glucose content detection

Cellular glucose content was quantified using the CheKine™ Glucose Content Assay Kit (Micromethod) (Abbkine, KTB1300). Lysates from treated/control cells were centrifuged to collect supernatants. Standard curves were generated via gradient-diluted glucose standards. Samples were mixed with the kit reagents and heat-treated (100 °C, 5 min), and the absorbance was measured at 630 nm using a microplate reader.

RNA immunoprecipitation (RIP)

RIP was performed using the PureBinding® RNA Immunoprecipitation Kit (GENESEED, P0101). Following insulin resistance induction, the cell lysates were incubated with protein A/G magnetic beads pre-coupled with 5 μ g of m⁶A antibody (Abcam, ab284130) or rabbit IgG control for 2 h at 25 °C with rotation. Antibody-bead complexes were washed,

then combined with lysate supernatants and rotated overnight at 4 °C (10 rpm). After magnetic separation and three wash cycles, bound RNA was extracted using kit protocols and stored at –80 °C. Reverse transcription qPCR was conducted as previously described.

MIAA intervention in an insulin-resistant cell model

THLE-2 cells at 90% confluency were treated with 0, 1, 2, 3, 4, 5, 6, or 7 μM MIAA for 24 h. Cell viability was assessed via the MTS assay, with 5 μM MIAA selected for subsequent experiments.

Cell transfection

Gene-specific siRNAs (see Supplementary Table 9), which were synthesized by Genepharma, were transfected using Lipofectamine™ RNAiMAX reagent (Thermo Fisher, 13778075). For the 12-well plates, complexes containing 2 μL siRNA and 4 μL transfection reagent in 200 μL Opti-MEM (Gibco, 31985070) were incubated with cells for 24 h. The cells were then expanded to 6-well plates for an additional 24 h prior to RNA extraction.

Liver cell line construction

FTO-knockout (KO) cells were generated using LentiCRISPRv2 (Addgene, 52961) with sgRNAs targeting conserved exons (sequences in Supplementary Table 9). Annealed sgRNA duplexes were cloned into Esp3I-linearized vector using DNA Ligation Kit (Takara, 6022Q), transformed into Trelief® 5α competent cells, and sequence-verified. For FTO/YTHDC1 overexpression and mutant constructs, target genes amplified from human cDNA were ligated into pCDH-CMV-MCS-EF1α-Puro using seamless cloning. Site-directed mutants were generated via PCR-mediated mutagenesis (primers in Supplementary Table 10 and 11) using Gibson assembly. Lentivirus was produced by co-transfecting 293 T cells with validated plasmids, psPAX2, and pMD2G. Viral supernatants collected at 48 h were used to infect THLE-2, followed by selection with 10 μg/mL puromycin. Monoclonal THLE-2 cells were established via limiting dilution and validated by western blot.

Statistics and reproducibility

All the results were expressed as the mean ± S.E.M. The exact sample size (n) for each experimental group was indicated in the figure legends. For correlation analysis, linear regression was performed. All statistical analyses were performed using GraphPad Prism 8. For comparisons between two unpaired independent groups, the two-tailed Student's *t*-test or the Mann-Whitney U test was used; Categorical data were analyzed by chi-square test; for comparisons of multiple groups, one-way ANOVA with Tukey's *post hoc* test or the Kruskal-Wallis test with Dunn's correction. Two-variable multi-group comparisons used two-way repeated-measures ANOVA with Sidak's/Tukey's *post hoc* tests. Statistical significance was defined as $P < 0.05$.

Reporting summary

Further information on research design is available in the Nature Portfolio Reporting Summary linked to this article.

Data availability

The datasets generated and analyzed during this study are included in the Supplementary Information. Source data underlying the figures are provided as a Source Data file accompanying this paper and are available from the corresponding authors upon reasonable request. The RNA-seq dataset has been deposited in the NCBI Sequence Read Archive (SRA) under BioProject accession number PRJNA1095170. The 16S rRNA sequencing data are publicly accessible through the NCBI BioProject database under accession number PRJNA980300. Metabolomics data have been deposited in the MetaboLights repository under accession code MTBLS13011. Source data are provided with this paper.

References

- Kerr, J. A. et al. Global, regional, and national prevalence of child and adolescent overweight and obesity, 1990–2021, with forecasts to 2050: a forecasting study for the Global Burden of Disease Study 2021. *Lancet* **405**, 785–812 (2025).
- Bendor, C. D., Bardugo, A., Pinhas-Hamiel, O., Afek, A. & Twig, G. Cardiovascular morbidity, diabetes and cancer risk among children and adolescents with severe obesity. *Cardiovasc. Diabetol.* **19**, 79 (2020).
- Jia, P. et al. Environmental determinants of childhood obesity: a meta-analysis. *Lancet Glob. health* **11**, S7–S7 (2023). **Suppl 1**.
- Marcus, C., Danielsson, P. & Hagman, E. Pediatric obesity-Long-term consequences and effect of weight loss. *J. Intern. Med.* **292**, 870–891 (2022).
- Jebeile, H., Kelly, A. S., O'Malley, G. & Baur, L. A. Obesity in children and adolescents: epidemiology, causes, assessment, and management. *Lancet Diab. Endocrinol.* **10**, 351–365 (2022).
- Cottone, P., Sabino, V., Nagy, T. R., Coscina, D. V. & Zorrilla, E. P. Feeding microstructure in diet-induced obesity susceptible versus resistant rats: central effects of urocortin 2. *J. Physiol.* **583**, 487–504 (2007).
- Liao, C. Y., Rikke, B. A., Johnson, T. E., Diaz, V. & Nelson, J. F. Genetic variation in the murine lifespan response to dietary restriction: from life extension to life shortening. *Aging Cell* **9**, 92–95 (2010).
- Speakman, J. R. & Mitchell, S. E. Caloric restriction. *Mol. Asp. Med.* **32**, 159–221 (2011).
- Cantoni, C., Dorsett, Y., Fontana, L., Zhou, Y. & Piccio, L. Effects of dietary restriction on gut microbiota and CNS autoimmunity. *Clin. Immunol.* **235**, 108575 (2022).
- Ruddick-Collins, L. C. et al. Timing of daily calorie loading affects appetite and hunger responses without changes in energy metabolism in healthy subjects with obesity. *Cell Metab.* **34**, 1472–1485.e1476 (2022).
- Ludwig, D. S., Hu, F. B., Lichtenstein, A. H. & Willett, W. C. Low-fat diet Redux at WHO. *Am. J. Clin. Nutr.* **118**, 849–851 (2023).
- Hageman, J. H. J. et al. The impact of dietary long-chain polyunsaturated fatty acids on respiratory illness in infants and children. *Curr. Allergy Asthma Rep.* **12**, 564–573 (2012).
- Schuchardt, J. P., Huss, M., Stauss-Grabo, M. & Hahn, A. Significance of long-chain polyunsaturated fatty acids (PUFAs) for the development and behaviour of children. *Eur. J. Child. s.* **169**, 149–164 (2010).
- Song, P. et al. The prevalence of vitamin a deficiency in Chinese children: a systematic review and Bayesian meta-analysis. *Nutrients* **9**, 1285 (2017).
- Xiong, Z. et al. Vitamin E and multiple health outcomes: an umbrella review of meta-analyses. *Nutrients* **15**, 3301 (2023).
- Ferraz-Bannitz, R. et al. Dietary protein restriction improves metabolic dysfunction in patients with metabolic syndrome in a randomized, controlled trial. *Nutrients* **14**, 2670 (2022).
- Solon-Biet, S. amanthaM. et al. The ratio of macronutrients, not caloric intake, dictates cardiometabolic health, aging, and longevity in Ad Libitum-fed mice. *Cell Metab.* **19**, 418–430 (2014).
- Richardson, N. E. et al. Lifelong restriction of dietary branched-chain amino acids has sex-specific benefits for frailty and life span in mice. *Nat. Aging* **1**, 73–86 (2021).
- Wu, H. et al. The gut microbiota in prediabetes and diabetes: a population-based cross-sectional study. *Cell Metab.* **32**, 379–390.e373 (2020).
- Bäckhed, F. et al. The gut microbiota as an environmental factor that regulates fat storage. *Proc. Natl. Acad. Sci. USA* **101**, 15718–15723 (2004).
- Goodrich, J. uliaK. et al. Human genetics shape the gut microbiome. *Cell* **159**, 789–799 (2014).

22. Shelton, C. D. et al. An early-life microbiota metabolite protects against obesity by regulating intestinal lipid metabolism. *Cell Host Microbe* **31**, 1604–1619.e1610 (2023).
23. Albenberg, L. G. & Wu, G. D. Diet and the intestinal microbiome: associations, functions, and implications for health and disease. *Gastroenterology* **146**, 1564–1572 (2014).
24. Schmidt, N. S. & Lorentz, A. Dietary restrictions modulate the gut microbiota: Implications for health and disease. *Nutr. Res.* **89**, 10–22 (2021).
25. Ruiz, A. et al. One-year calorie restriction impacts gut microbial composition but not its metabolic performance in obese adolescents. *Environ. Microbiol.* **19**, 1536–1551 (2017).
26. Wang, S. et al. Gut microbiota mediates the anti-obesity effect of calorie restriction in mice. *Sci. Rep.* **8**, 13037 (2018).
27. Li, G. et al. Intermittent fasting promotes white adipose browning and decreases obesity by shaping the gut microbiota. *Cell Metab.* **26**, 672–685.e674 (2017).
28. Zapata, R. C., Singh, A., Ajdari, N. M. & Chelikani, P. K. Dietary Tryptophan restriction dose-dependently modulates energy balance, gut hormones, and microbiota in. *Obes. -Prone Rats. Obes.* **26**, 730–739 (2018).
29. Castaño-Martínez, T. et al. Methionine restriction prevents onset of type 2 diabetes in NZO mice. *FASEB J.* **33**, 7092–7102 (2019).
30. Wang, L. et al. Methionine restriction alleviates high-fat diet-induced obesity: Involvement of diurnal metabolism of lipids and bile acids. *Biochim. Biophys. Acta (BBA) - Mol. Basis Dis.* **1866**, 165908 (2020).
31. Anthony, T. G., Morrison, C. D. & Gettys, T. W. Remodeling of lipid metabolism by dietary restriction of essential amino acids. *Diabetes* **62**, 2635–2644 (2013).
32. Wang, L. et al. Methionine restriction regulates cognitive function in high-fat diet-fed mice: roles of diurnal rhythms of SCFAs producing- and inflammation-related microbes. *Mol. Nutr. Food Res.* **64**, e2000190 (2020).
33. Tan, Y., Chrysopolou, M. & Rinschen, M. M. Integrative physiology of lysine metabolites. *Physiol. Genom.* **55**, 579–586 (2023).
34. Bazer, F. W., Wang, X., Johnson, G. A. & Wu, G. Select nutrients and their effects on conceptus development in mammals. *Anim. Nutr.* **1**, 85–95 (2015).
35. Gunarathne, R., Guan, X., Feng, T., Zhao, Y. & Lu, J. L-lysine dietary supplementation for childhood and adolescent growth: Promises and precautions. *J. Adv. Res.* **70**, 571–586 (2025).
36. Choi, P. M. et al. Population histamine burden assessed using wastewater-based epidemiology: The association of 1,4-methylimidazole acetic acid and fexofenadine. *Environ. Int.* **120**, 172–180 (2018).
37. Jiang, X. et al. The role of m6A modification in the biological functions and diseases. *Signal Transduct. Target. Ther.* **6**, 74 (2021).
38. Inge, T. H. et al. Five-year outcomes of gastric bypass in adolescents as compared with adults. *N. Engl. J. Med.* **380**, 2136–2145 (2019).
39. Griggs, C. L. et al. National trends in the use of metabolic and bariatric surgery among pediatric patients with severe obesity. *JAMA Child. s.* **172**, 1191–1192 (2018).
40. Kelly, A. S. et al. A randomized, controlled trial of liraglutide for adolescents with obesity. *N. Engl. J. Med.* **382**, 2117–2128 (2020).
41. Xiao, F. et al. Effects of essential amino acids on lipid metabolism in mice and humans. *J. Mol. Endocrinol.* **57**, 223–231 (2016).
42. Turnbaugh, P. J. et al. An obesity-associated gut microbiome with increased capacity for energy harvest. *Nature* **444**, 1027–1031 (2006).
43. Vrieze, A. et al. Transfer of intestinal microbiota from lean donors increases insulin sensitivity in individuals with metabolic syndrome. *Gastroenterology* **143**, 913–916 (2012).
44. Barcena, C. et al. Healthspan and lifespan extension by fecal microbiota transplantation into progeroid mice. *Nat. Med.* **25**, 1234–1242 (2019).
45. Parker, A. et al. Fecal microbiota transfer between young and aged mice reverses hallmarks of the aging gut, eye, and brain. *Microbiome* **10**, 68 (2022).
46. Mocanu, V. et al. Fecal microbial transplantation and fiber supplementation in patients with severe obesity and metabolic syndrome: a randomized double-blind, placebo-controlled phase 2 trial. *Nat. Med.* **27**, 1272–1279 (2021).
47. Le Roy, T. et al. *Dysosmobacter welbionis* is a newly isolated human commensal bacterium preventing diet-induced obesity and metabolic disorders in mice. *Gut* **71**, 534–543 (2022).
48. Hosomi, K. et al. Oral administration of *Blautia wexlerae* ameliorates obesity and type 2 diabetes via metabolic remodeling of the gut microbiota. *Nat. Commun.* **13**, 4477 (2022).
49. Qiao, S. et al. Gut *Parabacteroides merdae* protects against cardiovascular damage by enhancing branched-chain amino acid catabolism. *Nat. Metab.* **4**, 1271–1286 (2022).
50. Wang, K. et al. *Parabacteroides distasonis* alleviates obesity and metabolic dysfunctions via production of succinate and secondary bile acids. *Cell Rep.* **26**, 222–235.e225 (2019).
51. Wu, T.-R. et al. Gut commensal *Parabacteroides goldsteinii* plays a predominant role in the anti-obesity effects of polysaccharides isolated from *Hirsutiella sinensis*. *Gut* **68**, 248–262 (2019).
52. Li, T. et al. A gut microbiota-bile acid axis promotes intestinal homeostasis upon aspirin-mediated damage. *Cell Host Microbe* **32**, 191–208.e199 (2024).
53. Sakamoto, M. & Benno, Y. Reclassification of *Bacteroides distasonis*, *Bacteroides goldsteinii* and *Bacteroides merdae* as *Parabacteroides distasonis* gen. nov., comb. nov., *Parabacteroides goldsteinii* comb. nov. and *Parabacteroides merdae* comb. nov. *Int. J. Syst. Evolut. Microbiol.* **56**, 1599–1605 (2006).
54. Bryant, N. J., Govers, R. & James, D. E. Regulated transport of the glucose transporter GLUT4. *Nat. Rev. Mol. Cell Biol.* **3**, 267–277 (2002).
55. Yang, Q. et al. Serum retinol binding protein 4 contributes to insulin resistance in obesity and type 2 diabetes. *Nature* **436**, 356–362 (2005).
56. Shepherd, P. R. & Kahn, B. B. Glucose transporters and insulin action-implications for insulin resistance and diabetes mellitus. *N. Engl. J. Med.* **341**, 248–257 (1999).
57. Liu, H. et al. ALKBH5-mediated m⁶A demethylation of GLUT4 mRNA promotes glycolysis and resistance to HER2-targeted therapy in breast cancer. *Cancer Res.* **82**, 3974–3986 (2022).
58. Loos, R. J. F. & Yeo, G. S. H. The bigger picture of FTO—the first GWAS-identified obesity gene. *Nat. Rev. Endocrinol.* **10**, 51–61 (2013).
59. Wang, L. et al. NADP modulates RNA m⁶A methylation and adipogenesis via enhancing FTO activity. *Nat. Chem. Biol.* **16**, 1394–1402 (2020).
60. Frayling, T. M. et al. A common variant in the FTO gene is associated with Body Mass Index and predisposes to childhood and adult obesity. *Science* **316**, 889–894 (2007).
61. Zaccara, S., Ries, R. J. & Jaffrey, S. R. Reading, writing and erasing mRNA methylation. *Nat. Rev. Mol. Cell Biol.* **20**, 608–624 (2019).
62. Javier Ruiz-Ojeda, F., Plaza-Díaz, J., José Saez-Lara, M. & Gil, A. Effects of sweeteners on the gut microbiota: a review of experimental studies and clinical trials. *Adv. Nutr.* **10**, S31–S48 (2019).
63. Roze, M. et al. Impact of Maltitol and Sorbitol on technological and sensory attributes of biscuits. *Foods* **10**, 2545 (2021).
64. Quilez, J., Bullo, M. & Salas-Salvado, J. Improved postprandial response and feeling of satiety after consumption of low-calorie

- muffins with maltitol and high-amylose corn starch. *J. Food Sci.* **72**, S407–S411 (2007).
65. Dokoshi, T. et al. Dermal injury drives a skin to gut axis that disrupts the intestinal microbiome and intestinal immune homeostasis in mice. *Nat. Commun.* **15**, 3009 (2024).
66. Song, Y. L. et al. *Bacteroides goldsteinii* sp. nov.” isolated from clinical specimens of human intestinal origin. *J. Clin. Microbiol.* **43**, 4522–4527 (2005).
67. Meng, Q., Zhong, S., Wang, J., Gao, Y. & Cui, X. Advances in chitosan-based microcapsules and their applications. *Carbohydr. Polym.* **300**, 120265 (2023).
68. Zhang, H. et al. SUMOylation modification of FTO facilitates oxidative damage response of arsenic by IGF2BP3 in an m⁶A-dependent manner. *J. Hazard. Mater.* **472**, 134440 (2024).

Acknowledgements

This research was supported by the National Natural Science Foundation of China (Grant number: 82473594 to C.Z.C.), Chongqing Natural Science Foundation Innovation and Development Joint Fund Project (CSTB2023NSCQ-LZX0059 to C.Z.C.), Program for Youth Innovation in Future Medicine, Chongqing Medical University (W0043 to C.Z.C., W0054 to Q.L.). Chongqing Medical Scientific Research Project, Joint project of Chongqing Health Commission and Science and Technology Bureau (2023DBXM006 to C.Z.C.). Chongqing Medical University-Postdoctoral Research Start-up Fund (R4039, to F.Z.).

Author contributions

Conceptualization, C.Z.C., Z.Z. and F.Z.; Methodology, F.Z., Z.Y.L., J.Z., J.W. and Y.H.W.; Investigation, W.J.L., X.J.J., A.K., J.W.Y. and H.Y.Z.; Resources, Q.L. and J.F.Q.; Visualization, F.Z., Z.Y.L. and J.W.; Writing-Original Draft, F.Z., Z.Y.L. and J.W.; Writing-Review & Editing, C.Z.C., F.Z., Z.Y.L. and M.N.R.; Funding Acquisition, C.Z.C. and Z.Z.; Supervision, C.Z.C.

Competing interests

The authors declare no competing interests.

Additional information

Supplementary information The online version contains supplementary material available at <https://doi.org/10.1038/s41467-025-64892-z>.

Correspondence and requests for materials should be addressed to Chengzhi Chen.

Peer review information *Nature Communications* thanks Aron Lukas Benzon Clementsen, Torben Rasmussen, and the other anonymous reviewer for their contribution to the peer review of this work. A peer review file is available.

Reprints and permissions information is available at <http://www.nature.com/reprints>

Publisher's note Springer Nature remains neutral with regard to jurisdictional claims in published maps and institutional affiliations.

Open Access This article is licensed under a Creative Commons Attribution-NonCommercial-NoDerivatives 4.0 International License, which permits any non-commercial use, sharing, distribution and reproduction in any medium or format, as long as you give appropriate credit to the original author(s) and the source, provide a link to the Creative Commons licence, and indicate if you modified the licensed material. You do not have permission under this licence to share adapted material derived from this article or parts of it. The images or other third party material in this article are included in the article's Creative Commons licence, unless indicated otherwise in a credit line to the material. If material is not included in the article's Creative Commons licence and your intended use is not permitted by statutory regulation or exceeds the permitted use, you will need to obtain permission directly from the copyright holder. To view a copy of this licence, visit <http://creativecommons.org/licenses/by-nc-nd/4.0/>.

© The Author(s) 2025